Front. Phys., 2011, 6(3): 271–293
DOI 10.1007/s11467-011-0182-3

REVIEW ARTICLE

Transport in graphene nanostructures

Christoph Stampfer[1,2,†], **Stefan Fringes**[1], **Johannes Güttinger**[2], **Francoise Molitor**[2], **Christian Volk**[1], **Bernat Terrés**[1], **Jan Dauber**[1], **Stephan Engels**[1], **Stefan Schnez**[2], **Arnhild Jacobsen**[2], **Susanne Dröscher**[2], **Thomas Ihn**[2], **Klaus Ensslin**[2]

[1] *JARA-FIT and II. Institute of Physics B, RWTH Aachen University, 52074 Aachen, and Peter Grünberg Institute (PGI-9), Forschungszentrum Jülich, 52425 Jülich, Germany*

[2] *Solid State Physics Laboratory, ETH Zurich, 8093 Zurich, Switzerland*

E-mail: [†] *stampfer@physik.rwth-aachen.de*

Received March 28, 2011; accepted April 25, 2011

Graphene nanostructures are promising candidates for future nanoelectronics and solid-state quantum information technology. In this review we provide an overview of a number of electron transport experiments on etched graphene nanostructures. We briefly revisit the electronic properties and the transport characteristics of bulk, i.e., two-dimensional graphene. The fabrication techniques for making graphene nanostructures such as nanoribbons, single electron transistors and quantum dots, mainly based on a dry etching "paper-cutting" technique are discussed in detail. The limitations of the current fabrication technology are discussed when we outline the quantum transport properties of the nanostructured devices. In particular we focus here on transport through graphene nanoribbons and constrictions, single electron transistors as well as on graphene quantum dots including double quantum dots. These quasi-one-dimensional (nanoribbons) and quasi-zero-dimensional (quantum dots) graphene nanostructures show a clear route of how to overcome the gapless nature of graphene allowing the confinement of individual carriers and their control by lateral graphene gates and charge detectors. In particular, we emphasize that graphene quantum dots and double quantum dots are very promising systems for spin-based solid state quantum computation, since they are believed to have exceptionally long spin coherence times due to weak spin–orbit coupling and weak hyperfine interaction in graphene.

Keywords graphene, nanostructures, electron transport, quantum dots

PACS numbers 71.15.Mb, 78.30.Na, 81.05.Uw, 63.20.Kr

Contents

1 Introduction 271
2 Transport in bulk graphene revisited 273
2.1 Mobility 274
2.2 Minimum conductivity 274
2.3 Anomalous quantum Hall effect 274
3 Fabrication of graphene nanodevices 275
3.1 Mechanical exfolitation of graphite 275
3.2 Identification of graphene 275
3.2.1 Visibilty of graphene 276
3.2.2 Raman imaging 276
3.3 Etching graphene nanostructures 277
3.4 Contacting graphene nanodevices 277
4 Graphene nanoribbons 278
4.1 Energy gaps in graphene nanoribbons 278
4.1.1 Transport gap in back gate 279
4.1.2 Energy gap in bias direction 280
4.1.3 Energy scales as function of geometry 280
4.2 Coulomb blockade in nanoconstrictions 281
5 Graphene quantum dots 282
5.1 Graphene single electron transistor 282
5.2 Nanoribbon based charge detection on SETs 285
5.3 Electron–hole crossover in graphene quantum dots 286
5.4 Graphene double quantum dots 288
6 Conclusions 289
References 290

1 Introduction

Graphene, the first truly two-dimensional (2-D) crystal consists of a honeycomb-like hexagonal lattice of carbon

atoms. The carbon atoms form strong covalent bonds by three in-plane sp^2 hybridized orbitals, whereas the fourth valence electron of the $2s^2 2p^2$ orbitals of carbon, assigned to the perpendicular $2p_\perp$ orbital can move freely in plane forming the so-called π-electronic system [1]. The delocalized π-electronic states are responsible for electrical conductance and make graphene, in contrast to sp^3-hybridized insulating diamond, to a semimetal. In particular, the π-electronic system in combination with the hexagonal lattice, where two carbon atoms sit in the unit cell [see A and B in Fig. 1(a), where the dashed lines mark the unit cell], lead to a number of unique electronic properties of graphene [2–4]. The electronic band structure can be approximated by a nearest neighbor tight-binding approach of linear combinations of the perpendicular $2p_\perp$ orbitals. According to Wallace [2], this leads to $E(\boldsymbol{k}) = E_0 \pm \left|\sum_{i=1}^{3} \gamma_i \exp\left(-\mathrm{i}\boldsymbol{k}\cdot\boldsymbol{r}_i\right)\right|$, [illustrated in Fig. 1(b)], where $\gamma_i \approx 2.8$ eV [5] are the so-called nearest-neighbor hopping integrals, E_0 is the energy of the bare $2p_\perp$ orbital, and $\boldsymbol{r}_i$ are the vectors pointing to the three A atoms neighboring each B atom [see arrows in Fig. 1(a)]. The two freely moving valence electrons per unit cell completely fill the valence π-band and leave the conduction π^*-band unfilled resulting in a point-like Fermi surface [see Fig. 1(b)]. Therefore, in the near vicinity of the Fermi energy, the band structure of graphene [2, 6] can be linearized, leading to two cone-like structures centered at the two inequivalent so-called K and K' points at the corners of the hexagonal Brillouin zone [see Fig. 1(b)]. Consequently, the dynamics of charge carriers in graphene can be described in the near vicinity of the Fermi energy by a linear dispersion relation, $E(\boldsymbol{\kappa}) = \hbar v_\mathrm{F}|\boldsymbol{\kappa}|$ (and $\boldsymbol{\kappa} = \boldsymbol{k} \pm \boldsymbol{K}$), where the carriers behave like massless particles with a constant Fermi velocity $v_\mathrm{F} \approx 10^6$ m/s, about 300 times smaller than the speed of light [7–9]. Additionally, the presence of the two sublattices [A and B in Fig. 1(a)], due to the two carbon atoms per unit cell, allows to express the wavefunction for a unit cell by $\Phi = c_\mathrm{A}\Phi_\mathrm{A} + c_\mathrm{B}\Phi_\mathrm{B}$, where $\Phi_\mathrm{A,B}$ are the $2p_\perp$ wave functions at the A and B site and the two component vector (c_A, c_B) forms the so-called pseudo-spin in graphene. Indeed, in close analogy to neutrino physics [10], the dynamics of electrons in the near vicinity of the K points can be fully described by the Dirac–Weyl Hamiltonian, $H = v_\mathrm{F}\sigma\cdot\boldsymbol{p}$, where σ are the 2-D Pauli spin matrices and $\boldsymbol{p} = \hbar\boldsymbol{\kappa}$ is the momentum operator. Here, the graphene pseudo-spin takes the role of "real" spin in the neutrino system. The pseudo-spin up (or down) state is related to an A–B symmetric (or antisymmetric) wave function. Since the symmetry of these wave functions is a function of the $\boldsymbol{\kappa}$-vector direction, helicity ($h = \sigma\cdot\boldsymbol{p}/2|\boldsymbol{p}|$) becomes a good quantum number $h_{1,2} = \pm 1/2$ [10, 11]. Therefore, electrons (holes) around the K-point have a positive (negative) helicity. This implies that σ has its two eigenvalues either in the direction (+) or opposite (−) to the momentum $\boldsymbol{p}$. In other words, charge carriers in graphene can be described in terms of 2-D massless Dirac fermions [12–15]. Thus, the carriers can be considered as behaving analogously to relativistic particles but with a strongly reduced velocity allowing for the observation of quantum electrodynamic (QED)-specific phenomena in a solid-state environment [4].

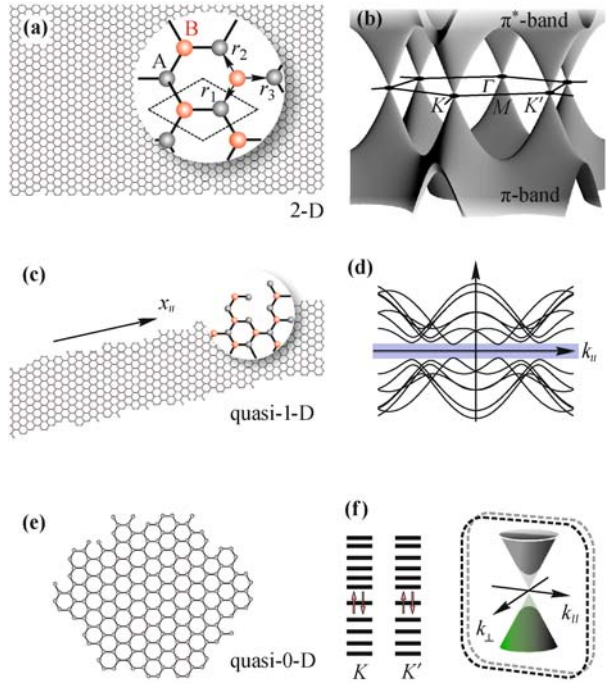

Fig. 1 **(a)** Illustration of truly 2-D graphene consisting of a honeycomb-like hexagonal lattice with two sublattices A and B (inset). The unit cell is marked by dashed lines. **(b)** Dispersion relation of graphene. The π- and π^*-band touch at the K and K' points. **(c)** Quasi-1-D nanoribbon with rough edges. At the edges, the A–B symmetry is broken (inset). **(d)** Schematic illustration of the quasi-1-D band structure of a nanoribbon (localized states not shown). The left panel illustrates the zone-folding approach. **(e)** Quasi-0-D graphene quantum dot made out of a nanometer-sized graphene flake with badly defined edges. **(f)** Expected energy levels of an ideal graphene quantum dot with depicted spin and valley (K and K') degeneracy.

This has also important impact on the transport properties of graphene. For example, the helicity as a good (quasi-particle) carrier quantum number completely blocks direct backscattering by long-range disorder [11]. This is due to low-momentum (low-$\boldsymbol{k}$) scattering processes, which only involve a single dispersion cone. There, direct backscattering processes would also require the transition from a symmetric to an antisymmetric wavefunction, which is not included in long-range Coulomb scattering. This leads to unprecedented carrier mobilities of up to 40 000 $\mathrm{cm}^2/(\mathrm{V\cdot s})$ [16] even at room temperature or up to 200 000 to 1 000 000 $\mathrm{cm}^2/(\mathrm{V\cdot s})$ in suspended graphene at low temperatures [17–20], making graphene a promising material for high mobility nanoelectronic applications. Pseudo-relativistic Klein tun-

neling [21–23] and related phenomena make it hard to confine carriers by electrostatic potentials. The so-called Klein paradox [24, 25] that refers to the transmission of relativistic particles through high and wide potential barriers is an exotic and counterintuitive consequence of QED [23]. The chiral nature of the quasi-particles in graphene leads to a matching between electron and hole (i.e., QED-positron) wavefunctions across the potential barrier resulting in a high-probability tunneling. Therefore, it has been suggested to use graphene barriers rather for the realization of electronic lenses, e.g., a Veselago lens [26]. On the other hand, the roughness of the edge potentials will make it difficult to observe quantized conductance in 1-D graphene structures [27]. Furthermore, the cyclotron energy of Dirac fermions scales like $\sqrt{B}$ (where B is the magnetic field), in contrast to the linear behavior for particles with parabolic dispersions [4]. This leads to very different cyclotron energy scales in graphene compared to standard semiconductors, which makes it possible to observe the quantum Hall effect even at room temperature [28]. However, not only the energy scale and B-field dependence differ from the ordinary 2-D electron gas but there is also an anomalous "half-integer" quantum Hall effect with a level at zero energy (i.e., at the so-called Dirac point) that includes both hole and electron states [12, 13]. This is related to the coupling of the pseudo-spin with orbital motion giving rise to a geometric phase of π [29] (the so-called Berry phase [30]) accumulated along cyclotron trajectories [12, 13, 31]. For more comprehensive reviews about properties of bulk graphene, please refer to Refs. [3, 4, 7, 9, 32–34].

In addition to its unique electronic – purely charge based – properties, graphene and carbon materials in general have promising electron spin properties. It is believed that electrons in these materials have exceptionally long spin decoherence times due to weak spin–orbit interactions (light weight of carbon) [35, 36] and weak hyperfine coupling due to the low nuclear spin concentration, arising from the 99% natural abundance of ^{12}C [37]. This promises spin decoherence times superior to the GaAs material system in which solid-state spin qubits are most advanced today [38, 39], making graphene in particular interesting as the host material for quantum dots where individual electron spins could be used as spin-qubits [37]. Spin–qubits are considered as promising building blocks for future quantum computation or information processing in general. However, in contrast to the state-of-the-art semiconductor (e.g., GaAs) quantum dots, the electron confinement in gapless graphene is rather challenging and needs novel technological approaches for fabricating low-dimensional graphene nanostructures. Here, we review work on the fabrication and characterization of graphene nanostructures. We discuss quasi-1-D nanoribbons consisting of etched graphene strips with rough edges [see Fig. 1(c)]. These systems are expected to exhibit a washed out linear 1-D density of states and a band structure similar to carbon nanotubes [1] [Fig. 1(d)], where an effective transport gap is observed near the charge neutrality point. Furthermore, we focus on quasi-0-D graphene quantum dots [Fig. 1(e)] with discrete energy levels, as illustrated in [Fig. 1(f)]. In this context, we discuss the tunability of graphene single-electron transistors, transport via quantum confined excited states, and charge detection by using a nearby nanoribbon. This review follows partly Ref. [40] and it is organized as follows: We start with Section 1 by reviewing the transport properties of 2-D graphene. In Section 2, the fabrication of graphene nanodevices is described in detail. Section 3 focuses on graphene nanoribbons and Section 4 on graphene quantum dots.

2 Transport in bulk graphene revisited

Electronic transport experiments allow to probe electronic properties in the vicinity of the Fermi level. At sufficiently low temperatures, this provides direct insights into the electronic density of states, carrier densities, and mobilities. In the context of diffusive transport, the zero-temperature conductivity can be expressed according to the Drude model by $\sigma(E_{\rm F}) = n(E_{\rm F})e\mu(E_{\rm F})$, where n is the carrier density (i.e., the integrated density of states) and μ is the mobility [41]. By varying the Fermi energy, $E_{\rm F}$, for example by applying a global electrostatic potential, we can study the conductivity as a function of $E_{\rm F}$ obtaining insights into mobility and band structure properties [42]. An established method to experimentally characterize the electronic transport properties of quasi-2-D materials is based on the so-called Hall bar geometry, as shown in the inset of Fig. 2(a). By injecting a current from the left most to the right most contact, the longitudinal resistance can be extracted in a four point measurement geometry by recording the potential drop between two side contacts. Additionally, one can measure the transverse Hall resistance in weak (and strong) magnetic field, which allows to deduce the carrier density n and the mobility μ, independently. A global back gate [separated by $d \approx 300$ nm thick silicon oxide (SiO_2)] is commonly used to tune the overall Fermi level. The influence of an applied back gate voltage V_{bg} on the carrier density in bulk graphene can be described by a simple parallel-plate capacitor model. The induced charge carrier density as function of applied back gate voltage is then given by $n(V_{bg}) = \alpha V_{bg}$, where $\alpha = \epsilon_0\epsilon_{ox}/(de) = 7.4 \times 10^{10}$ cm$^2\cdot$ V^{-1}. Using this model, the mobility can be extracted from the four-point longitudinal graphene Hall bar conductivity measurement shown in Fig. 2(a). The conductivity minimum at roughly $V_{bg}^{\rm D}$ =10 V reflects the Dirac (or charge neutrality) point, where the carrier

density is lowest. For ideal 2-D graphene, theory actually predicts a vanishing carrier density. The back gate voltage offset from 0 V is due to unintentional p-doping of the graphene sample during fabrication (see [43–45]). By applying a more positive voltage $V_{bg} > V_{bg}^{\mathrm{D}}$ the electron density increases and the conductivity increases linearly in V_{bg}. Similarly, we find for $V_{bg} < V_{bg}^{\mathrm{D}}$ the regime of hole transport, where the conductivity also increases linearly as a function of $|V_{bg}|$.

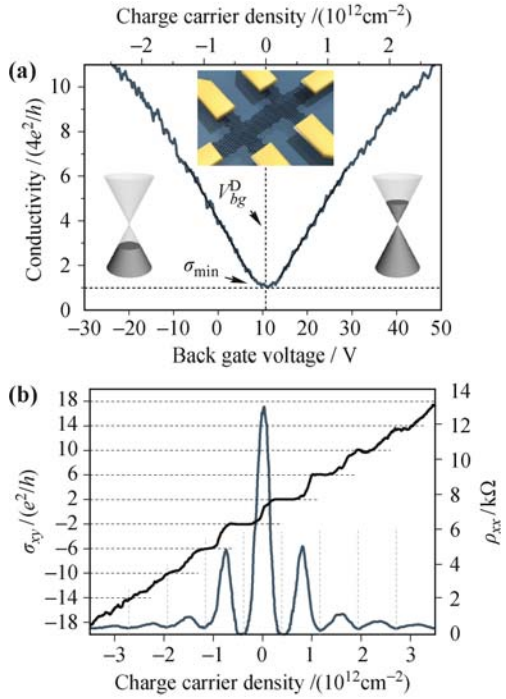

Fig. 2 **(a)** Conductivity as a function of back gate voltage V_{bg} and carrier density n measured on a graphene hall bar, as illustrated by the central inset. Transport can be tuned from the hole (*left*) to the electron (*right*) regime by crossing the so-called Dirac point, V_{bg}^{D} , with a minimum conductivity of approx imate $4e^2/h$. (Source drain current $I_{\mathrm{sd}} = 20$ nA rms.) **(b)** Hall conductivity σ_{xy} (*black curve*) and longitudinal resistivity σ_{xx} (*blue curve*) plotted as a function of charge carrier density at $B = 8$ T. The typical half-integer quantum Hall plateaus for graphene are observed. The vertical dashed lines indicate the filling factors of the Landau levels obtained theoretically, in good agreement with the experiment ($I_{\mathrm{sd}} = 100$ nA rms). Reproduced from Ref. [46], Copyright © 2007 American Physical Society.

2.1 Mobility

From the linear slopes of the conductivity versus back gate voltage trace, we can extract the carrier mobilities for both the electron and hole regimes. The presented measurements belong to a characteristic sample with a density-independent mobility close to 5000 $\mathrm{cm}^2/(\mathrm{V{\cdot}s)}$ for both carrier types. For a charge carrier density of $|n| = 10^{12}\,\mathrm{cm}^{-2}$, this corresponds to a mean free path $\lambda_m = \hbar\mu\sqrt{\pi n}/|e| \approx 60$ nm, which is consistent with the assumption that transport in the micrometer-sized Hall bar can be considered as diffusive [42, 46]. The measured mobility in graphene on SiO_2 substrates has been found to be mainly temperature independent and might be limited by (i) warping and ripples (or frozen phonons) [47] (ii) strong doping fluctuations [43, 48], or (iii) electron–hole puddles [49]. In contrast, high-quality graphene samples on hexagonal boron nitride substrate exhibit at room temperature a mobility of 40 000 $\mathrm{cm}^2/(\mathrm{V{\cdot}s)}$ which at low temperature (2 K) increases up to 80 000 $\mathrm{cm}^2/(\mathrm{V{\cdot}s)}$ [16]. Measurements on freely suspended graphene have exhibited mobilities as high as 200 000 to 1 000 000 $\mathrm{cm}^2/(\mathrm{V{\cdot}s)}$ (at 2 K) [17–20]. The mobility in suspended graphene exhibits a strong temperature dependence indicating that phonons (i.e., frozen phonons in non-suspended graphene) are playing an important role. Along this line, it has been found very recently that flexural phonons may limit the mobility of suspended graphene to values on the order of 10 000 $\mathrm{cm}^2/(\mathrm{V{\cdot}s)}$ [20].

2.2 Minimum conductivity

Another important observation is that the minimum conductivity σ_{min} in bulk graphene samples does not disappear in the limit of vanishing $\langle n \rangle$ but rather tends to a minimum value of the order of the quantum unit e^2/h [50, 51]. This quantum-limited conductivity is an intrinsic property of 2-D Dirac fermions, which persists in ideal graphene crystals without any impurities or lattice defects [8, 50, 52–56]. The experimentally observed conductivity minima σ_{min} depend on sample geometry, disorder (i.e., doping fluctuations and electron–hole puddles), and overall doping of the graphene flake [3, 51]. Several experiments [3, 51, 57, 58] on samples with similar geometries show such a minimum conductance value. The presence of the conductivity minimum σ_{min} has major impact on the electrostatic tunability of graphene devices [42], making it difficult to fully pinch off currents in 2-D graphene devices.

2.3 Anomalous quantum Hall effect

One of the most spectacular transport phenomenon reported so far is the well-understood anomalous half-integer quantum Hall effect (QHE) reflecting the consequences of graphene's QED-like energy spectrum. Figure 2(b) shows the QHE of single-layer graphene [12, 13, 46, 59, 60], which is the relativistic counterpart of the well-known integer QHE observed in semiconductors with a band gap and a parabolic dispersion [61]. It manifests itself as a continuous ladder of equidistant plateaus in Hall conductivity σ_{xy}, which persists through the neutrality (Dirac) point. There a charge carrier crossover from electrons to holes takes place. The sequence of plateaus is shifted with respect to the standard QHE ladder by 1/2. The plateaus arise at $\sigma_{xy} = \pm 4e^2/h(N + 1/2)$, where N is the Landau level index and the factor 4 appears

due to twofold valley (K and K') and twofold spin degeneracy. The unusual sequence arises from the QED-like quantization of graphene's electronic energy spectrum in magnetic field B, given by $E_N = \pm v_F\sqrt{2e\hbar BN}$, where the sign $\pm$ refers to electrons and holes, respectively [54, 62–64]. The existence of the quantized level at zero energy $N = 0$ ($V_{bg} = V_{bg}^D$), which is shared by electrons and holes, is essentially everything one needs to explain the anomalous QHE [12, 13]. Consequently, the measurement shown in Fig. 2(b) also provides a clear fingerprint for distinguishing between single- and multi-layer graphene [3]. More recently, measurements on ultraclean freely suspended graphene samples have even exhibited the fractional quantum Hall effect [65] in graphene [66, 67]. It has been shown that at low carrier density graphene becomes an insulator with a magnetic-field-tunable energy gap. These newly discovered quantum states offer the opportunity to study correlated Dirac fermions in graphene in the presence of large magnetic fields [67].

3 Fabrication of graphene nanodevices

The state-of-the-art fabrication of graphene devices and particular of graphene nanodevices has been mostly developed in Manchester by Geim and Novoselov [12, 42] and at Columbia University by Kim and colleagues [13]. In Fig. 3 we summarize the different process steps. The substrate material consists of highly doped silicon (Si^{++}) bulk material covered with around 90 or 300 nm of silicon oxide (SiO_2), where thickness and roughness of the SiO_2 top layer is crucial for the identification and further processing of single-layer graphene samples (a). Before depositing graphene, standard photolithography followed by metallization (usually chrome/gold) and lift-off is used to pattern arrays of reference alignment markers on the substrate in order to reidentify locations (for addressing individual graphene flakes) on the chip (b). For a general review on micro-fabrication, please refer to Ref. [68].

3.1 Mechanical exfolitation of graphite

The deposition of graphene, including also few-layer graphene flakes is based on mechanical exfoliation of (natural) graphite by adhesive tapes [42]. In 2005, two groups [12, 13] proved that this simple technique indeed leads to high-quality single-layer graphene flakes resting on the SiO_2 surface. Hereby, natural graphite flakes are distributed on a sticky (e.g. scotch) tape followed by folding this tape several times, such that the stacked graphene sheets are pulled apart leading to thinner and thicker few-layer graphene and ultimately to single-layer graphene sheets. In a next step, the Si/SiO_2 dies get pressed hard onto the tape in order to transfer the carbon material from the adhesive tape to the SiO_2 surface.

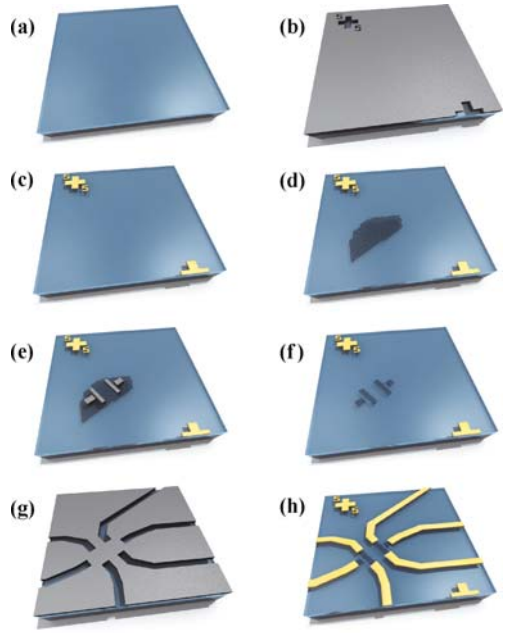

Fig. 3 Fabrication process: **(a)** Starting point is a silicon substrate with a 290 nm thick silicon dioxide on top. **(b)** With optical lithography orientation numbers for the flakes and markers used for the alignment during the subsequent electron beam lithography (EBL) steps, are written into the photo resist. **(c)** The structure is then made with evaporation of chromium and gold, followed by a lift-off process. **(d)** Deposition of graphene on the substrate and identification of single-layer flakes using an optical microscope and Raman spectroscopy. **(e)** and **(f)** Patterning of the flakes by EBL and reactive ion etching (RIE). **(g)** An additional EBL step is performed for defining the contacts, which are then made by evaporation of chromium and gold, followed by a lift-off process. **(h)** Final device, ready for bonding. Reproduced from Ref. [128], Copyright © 2010 Institute of Physics.

Since the early investigations of the first isolated graphene prepared by this rather dirty and unreliable mechanical exfoliation of graphite crystals, many chemical approaches to synthesize large-scale graphene have been developed, including epitaxial growth on silicon carbide [69, 70] and ruthenium [71], nickel [72] or copper [73], as well as 2-D assembly of reduced graphene oxides [74]. These are very active research areas and wafer-scale single-layer graphene might be in reach soon.

3.2 Identification of graphene

After exfoliation and deposition, there are graphite flakes with all kinds of layer thicknesses on the sample. The main difficulty is to find the thinnest among them (i.e., the single-layer graphene). Surprisingly, an optical microscope in combination with a carefully selected oxide thickness is sufficient for finding individual graphene flakes. This technique is widely used for the identification of graphene flakes because optical microscopy in contrast to scanning force microscope (SFM) and Raman imaging techniques (e.g., [75]) provides sufficient throughput for

scanning large samples. However, an optical image cannot unambiguously distinguish between single- and bilayer graphene. Therefore, Raman spectroscopy [76–78] and SFM techniques are indispensable for fully characterizing graphene flakes.

3.2.1 Visibilty of graphene

The optical visibility of graphene on various substrates (including SiO_2) can be well understood in terms of a Fresnel-law-based model [79–82]. Thin graphite flakes are sufficiently transparent to add to an optical path, which changes their color by interference with respect to an empty wafer [42, 80]. For a certain thickness of SiO_2, even a single-layer was found to give sufficient, albeit faint, contrast to allow the huge image processing power of the human brain to spot in seconds, a few micron-sized graphene crystallites among copious thicker flakes scattered over a millimeter-sized area. The origin of the detectable optical contrast is not only due to an increased optical path but also due to the notable opacity of graphene. The intensity of the reflected light can be described by the Fresnel law. For green light (550 nm) at which human eyes are most sensitive, the contrast is maximized by using an silicon oxide thickness of approximate 90 or 300 nm [80]. Since there is a strong dependence on the oxide thickness, it is necessary to have an accurate and homogeneous thickness over the wafer for providing a homogenous visibility of graphene. In summary, the strong dependence on the substrate material and the light source (including filtering) make it very hard to clearly distinguish between single- and few-layer graphene. Thus, optical microscopy is good for finding the location of a potential single-layer graphene flake. However, full characterization and clear fingerprint for single-layer graphene has to be provided by an additional technique.

3.2.2 Raman imaging

Raman spectroscopy has been identified to be a powerful tool to unambiguously distinguish between single- and few-layer graphene [76–78]. The 2-D nature of graphene has pronounced effects not only on their electronic band structure but also on their vibrational properties. Spectroscopic work on carbon materials has become extremely rewarding as it provides fundamental insight as well as the information used to characterize graphene [43, 83]. Since the resonant Raman-scattering signal of carbon materials (for a review see [84–86]) is so large that even individual micron-sized graphitic flakes can be investigated, it has become an *in-situ* nondestructive tool for its characterization. Without going into too many details here, the Raman spectra provide a clear fingerprint of single-layer graphene including three main peaks.

One distinguishes three peak families in the Raman spectrum: i) The D mode peak at 1350 cm^{-1}, which does not originate from a Γ-point Raman active vibration, is induced by disorder including edges [78]. Therefore, the absence of this peak provides a good quality check of the deposited graphene material. ii) The high-energy mode (HEM) vibrations in sp^2 bound carbon materials correspond to the Γ-point optical phonon mode at 1582 cm^{-1}. The carbon atoms move tangentially to the graphene sheet and this so-called G-peak is prominent in graphite, nanotubes, and graphene. In the latter, it can be fitted nicely by a single Lorentzian peak. From the actual G-peak position, we gain direct insight into the doping level of the graphene flake [43, 83, 87–90]. iii) The double-resonant 2D peak [91], which is the overtone of the D mode, shifts at about twice the rate of the D mode (i.e., 2679 cm^{-1}). Since no defects are involved in this two-phonon scattering process, the 2D mode is always observed independently of the defect concentration (or edges) [92]. Moreover, the line shapes of the 2D peak also carry valuable information about the underlying electronic band structure [see Fig. 4(a)]. This is due to the large $-k$ phonons involved in this process, which resonantly connect the two cones at the inequivalent K-points. The number of possible phonon transitions is now directly linked with the number of electronic bands available. Thus, for single-layer graphene, only one band per valley is present and therefore only one D-phonon transition is possible. This leads to a perfect Lorentzian peak shape, as shown in the lower panel of Fig. 4(a). In

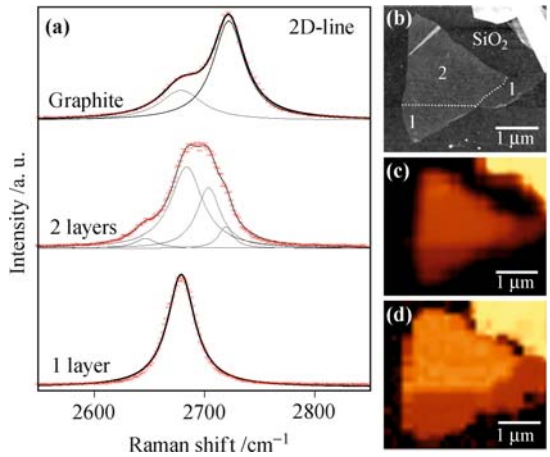

Fig. 4 **(a)** 2D Raman peaks for single- and bilayer graphene with graphite as reference. The dashed lines show the Lorentzian peaks used to fit the data, the solid lines are the fitted results. The single peak position for the single-layer graphene is at 2678.8 ± 1.0 cm^{-1}. The peak position of the two inner most peaks for double-layer graphene are 2683.0 ± 1.5 cm^{-1} and 2701.8 ± 1.0 cm^{-1}. **(b)** SFM micrograph of a graphitic flake consisting of one bi- and two single-layer sections (white dashed line along the boundaries), highlighted in the Raman map **(c)** showing the integrated intensity of the G line. **(d)** Raman mapping of the full width half maximum (FWHM) of the 2D line clearly showing the difference between single- and bi-layer regions. Reproduced from Ref. [78], Copyright © 2007 American Chemical Society.

contrast, due to the four carbon atoms per unit cell in bilayer graphene, we find two electronic bands per valley resulting in a total of four possible transitions and the 2D line shape indeed is composed of four individual Lorentzian peaks [see center panel in Fig. 4(a)]. Thus, the 2D line shape provides a strong fingerprint of graphene and is nowadays widely used for identifying graphene. For comparison, the upper panel of Fig. 4(a) shows the 2D peak of graphite. In Figs. 4(c) and (d), we show confocal Raman images of a graphitic flake with regions of single- and bi-layer. A corresponding SFM image is shown in Fig. 4(b). The laser-spot size is approx. 400 nm in diameter. The single- and bi-layer regions can be nicely resolved in both i) the G-peak intensity map [Fig. 4(c)] where mainly the different amount of carbon material (per spot size) enters and ii) the line width of the 2D-peak [Fig. 4(d)] which unambiguously pins down the single-layer region. Indeed, the line width of 33 cm^{-1} for single-layer graphene has also been shown to be doping independent [43] making this quantity a very reliable measure for identifying single-layer graphene.

3.3 Etching graphene nanostructures

For fabricating well-designed graphene nanodevices, a reliable technique to structure graphene is required. The commonly used technique is based on resist spin coating, electron beam lithography (EBL), development and subsequent etching of the unprotected graphene. This process sequence is illustrated in Fig. 3(d) through (f). The resist [mainly polymethyl methacrylate (PMMA)] thickness varies between 50 and 100 nm directly limiting on one hand the minimum feature size of the final graphene device and on the other hand the process window for the actual etching step. It has been found that short (5–15 s) mainly physical reactive ion etching (RIE) based on argon and oxygen (80/20) provides good results without influencing the overall quality of the flake [46, 93]. With reactive ion etching, the chemical bonds of the etch target are broken up by mainly physical bombardment with argon ions which were created in a plasma. On the bombarded sites, chemical etching (in our case with oxygen) can take place enhanced by the heightened chemical reactiveness of the etchant species due to the plasma. Hence, this process combines the anisotropic etching possibilities of the physical bombardment, with the material selectivity of the chemical etching. The ability of this process to etch up to around five-layer thick flakes facilitates contacting structures by reducing the risk for shorted contacts due to thicker graphitic regions. In Figs. 5(a)–(c), SFM images of a flake before (a) and after the RIE etching (c) is shown. In Fig. 5(b), the used etch mask is highlighted (see dashed lines). More advanced graphene nanostructures are shown in Figs. 5(e) and (f). Both structures have been fabricated by RIE etching as described above. In Fig. 5(e) we show a graphene quantum dot device with a nearby graphene charge detector and three lateral gates [94]. A similar device will be discussed in Section 5.2. In Fig. 5(f) a graphene ring is shown. On such ring devices Aharonov–Bohm oscillations [95] have been successfully demonstrated [96–98].

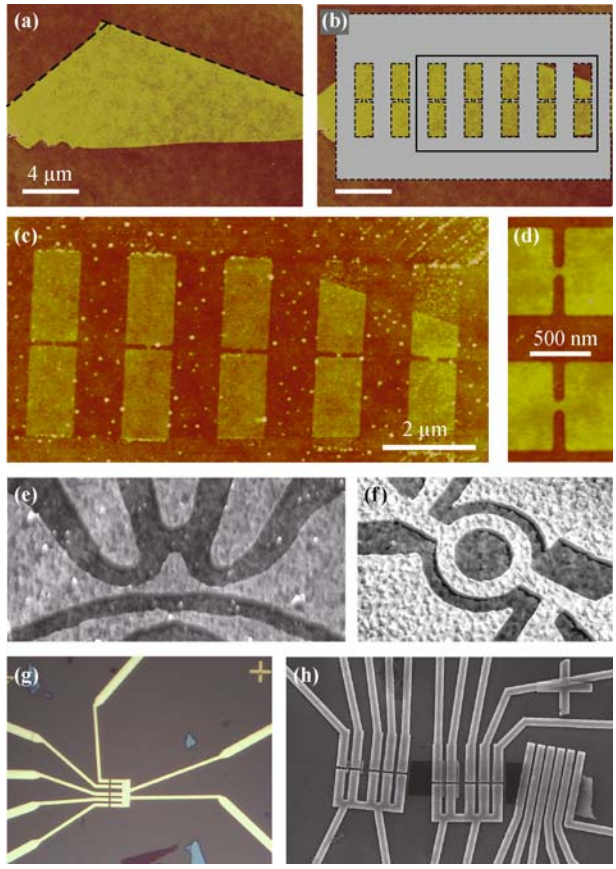

Fig. 5 **(a)** Scanning force microscope (SFM) image of a few-layer graphene flake before etching. **(b)** The very same image with the etch mask on top (see gray area) and **(c)** shows a scanning force microscope close-up [see black box in panel (b)] of the reactive ion etched graphene flake. **(d)** Highlights a close-up of etched nanoribbons [similar to devices shown in panel (c)]. **(e)** SFM image of a more advanced etched graphene nanostructure consisting of a graphene quantum dot with two narrow graphene constrictions, a close-by nanoribbon and three lateral gates. The smallest graphene structures are on the order of 30 nm. **(f)** SFM image of a graphene ring structure. The ring has an inner radius of about 200 nm and an outer radius of about 350 nm. On each end of the ring structure, there are two graphene contact pads and the two lateral side gates are located 100 nm away from the structure. **(g)** Light microscope image of metal electrodes contacting graphene structures. **(h)** Scanning electron microscope (SEM) image of contacted graphene nanostructures [similar devices as shown in panel (g)].

3.4 Contacting graphene nanodevices

After etching and removing the residual EBL resist, SFM images [as shown in Figs. 5(c) and (d)] are important for proving the quality of the patterned graphene flakes, mainly in terms of contamination. Here in particular the surface roughness of the flake, which should

be lower than 0.2 nm rms, is a good quality measure for flakes before contacting. Selected graphene nanostructures are next contacted by an additional EBL step, followed by metallization and lift-off, as illustrated in Fig. 3(f) through (h). Two layers of EBL resist are used to provide a T-shape resist profile allowing to pattern metal structures down to 70 nm in lateral dimension. After development, 2–5 nm chrome (Cr) or titanium (Ti) and 30–60 nm gold (Au) are evaporated for contacting the preselected graphene nanostructures. In Fig. 5(e), we show an optical microscope image of the metallic wiring of graphene nanostructures after successful lift-off process. SFM or scanning electron images [shown in Fig. 5(f)] proves that the alignment between graphene nanostructure and metal electrodes is sufficient for studying transport through these devices [see also Fig. 6(a)]. The sample is now ready for packaging and wire bonding, generally both are crucial and important steps for transport studies on nanodevices.

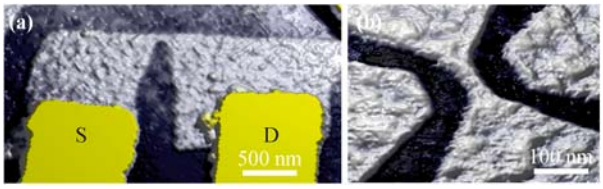

Fig. 6 **(a)** SFM image of a narrow graphene constrictions after contacting the flake to source (S) and drain (D) lead. The Cr/Au contacts are highlighted in yellow. **(b)** SFM image of a fabricated graphene nanoribbon with two side gates (see bright areas) resting on SiO_2 (dark areas). This nanoribbon has a width of $w \approx 30$ nm and a length of $l \approx 100$ nm. The white scale bar in this figure correspond to 100 nm and the black bar corresponds to 500 nm. Reproduced from Ref. [128], Copyright © 2010 Institute of Physics.

4 Graphene nanoribbons

Graphene nanoribbons [see Figs. 1(c), 5(c), 5(d) and 6], in contrast to bulk graphene, exhibit an effective energy gap [Fig. 1(d)], overcoming the gapless band structure of graphene [Fig. 1(b)]. Graphene nanoribbons, including graphene nanoconstrictions show an overall semiconducting ambipolar behavior, which makes these quasi-1-D graphene nanostructures promising candidates for the fabrication of nanoscale graphene transistors [99–103], tunnel barriers, single electron transistors [104–107], quantum dots [94, 108–113], and double quantum dot devices [114–117] as discussed in Section 5. On the other hand, ideal graphene nanoribbons [118–121] promise interesting quasi-1-D physics with strong relations to single-walled carbon nanotubes [1, 84]. Transport through graphene nanoribbons has been studied by a number of groups [122–131] and an interpretation of the experimentally observed transport and energy gaps in fabricated nanoribbons is discussed below. In Fig. 6, we show SFM images of fabricated graphene nanoribbons [124] with and without lateral graphene side gates. These structures were fabricated by using the technological methods and processes described in Section 3. For example, the device shown in Fig. 6(b) consist of a nanoribbon with length $l = 100$ nm and a width w of 50 nm. The graphene side gates are separated by a gap of 50 nm from the nanoribbon.

In Fig. 7(a) we show a typical low source-drain bias ($V_b = 300\ \mu\text{V} \ll 4k_BT$) back gate characteristic of a graphene nanoribbon ($w = 45$ nm; sample not shown) [125]. This measurement has been recorded at an electron temperature of ≈ 2 K. By comparing this measurement with the back gate characteristics of 2-D graphene [Fig. 2(a)], we find manifestations of the (quasi-1-D) nanoribbon size effects in the transport properties. Similar to the measurement shown in Fig. 2(a), we can tune transport from the hole (left side; see inset) to the electron regime (right side). In contrast to bulk graphene, where we find a linear dependence of the conductance (i.e., the current) on the back gate voltage (i.e., carrier density), here we find a sub-linear slope, an overall strongly reduced conductance, and reproducible fluctuations, which may be due to local resonances or attributed to conductance fluctuations [132]. In contrast to the conductance minimum ($\sigma_{\min} = 4e^2/h$) at the Dirac point observed in 2-D, we find a region of strongly suppressed current [see region 6 V $< V_{bg} <$ 12 V in Fig. 7(a)] around the charge neutrality point. This region of suppressed current is the so-called transport gap ΔV_{bg} in back gate voltage [$\Delta V_{bg} \approx$ 6 V, see also Fig. 7(d)]. In the following subsection (Subsection 4.1), we summarize the experimental observation of two different energy scales for the transport gap in both, the back gate and source–drain bias direction. In Subsection 4.2 we describe a simple model based on Coulomb blockade in disordered systems to explain the observed transport through fabricated graphene nanoribbons.

4.1 Energy gaps in graphene nanoribbons

In close analogy to carbon nanotubes, which can be considered as graphene stripes wrapped up to seamless cylinders [84], a number of theoretical predictions have been put forward to describe a (clean confinement) energy gap in graphene nanoribbons. Along these lines, zone folding approximations [119], π-orbital tight binding models [133, 134], and first-principles calculations [135, 136] predict an energy gap E_g scaling as $E_g = \alpha/w$ with the nanoribbon width w, where α is in the range of 0.2 eV·nm to 1.5 eV·nm, depending on the model and the crystallographic orientation of the graphene nanoribbon [27]. However, these theoretical estimates can neither explain the experimentally observed energy gaps of etched nanoribbons (with rough edges) of widths beyond 20 nm, which turn out to be significantly larger than predicted,

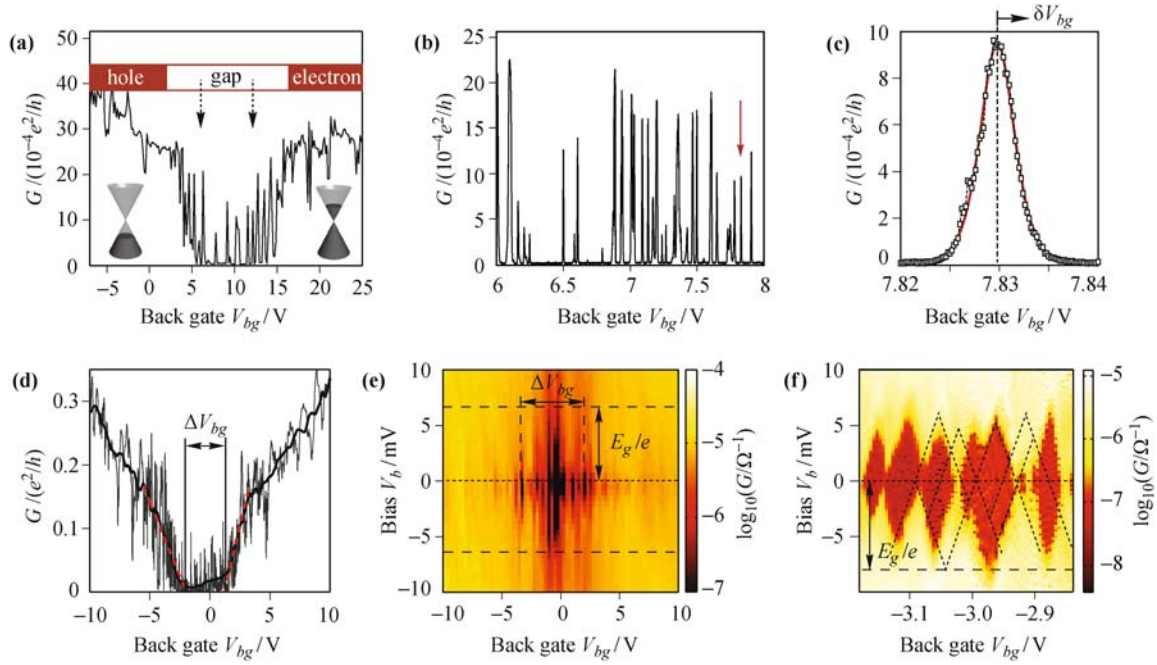

Fig. 7 Transport and energy gaps in graphene nanoribbons. **(a)** Low bias (V_b = 300 μV) back gate characteristics (of a nanoribbon with w = 45 nm) showing that the regimes of hole and electron transport are separated by the so-called transport gap, delimited by the vertical arrows. **(b)** High resolution close-up inside the gap displaying a large number of sharp resonances within the gap region. **(c)** Close-up of a single resonance [see arrow in panel (b)]. **(d)** Transport gap measurements for the constriction with dimensions w = 85 nm, l = 500 nm. Conductance versus back gate voltage V_{bg}, illustrating the procedure used to determine the size of the transport gap in back gate voltage ΔV_{bg}. The measurement is performed with a bias voltage of 300 μV. The trace form is smoothened over 2.5 V in V_{bg}. The black lines indicate the linear fits used to determine the gap size. **(e)** Color plot of the conductance as a function of applied back gate and bias voltage. **(f)** Zoom of the gap measured in (e). Reproduced from Refs. [124, 125], Copyright © 2009 American Physical Society.

nor do they explain the large number of resonances experimentally found inside the transport gap [see e.g., Fig. 7(b)] [122–127]. This has led to the suggestion that localized states and interaction effects due to edge roughness, disorder (e.g., bulk disorder), or bond contractions at the edges [137] may dominate the transport gap. Several mechanisms have been proposed to describe the observed gap, including re-normalized lateral confinement [123], quasi-1-D Anderson localization [138], percolation models [139], and many-body effects (including quantum dots) [140], where substantial edge roughness is required. It has also been shown that moderate amounts of edge roughness can substantially suppress the linear conductance near the charge neutrality point [141], giving rise to localized states relevant for both single-particle and many-body descriptions.

In contrast to the prediction of clean energy gaps (predicted for samples without bulk disorder and edge roughness), where transport should be completely pinched-off, transport experiments show a large number of reproducible conductance resonances inside the gap reminiscent of conductance resonances in the Coulomb blockade regime of quantum dots [Figs. 7(a) and (b)]. Sequences of resonances with small line widths indicate strong localization. An example of a particularly narrow resonance is shown in Fig. 7(c) [see arrow in Fig. 7(b)]. The line shape can be well fitted by $I \propto \cosh^2[e\alpha_{bg}\delta V_{bg}/(2.5k_BT_e)]$, where $\alpha_{bg} \approx 0.2$ is the back gate lever arm and $\delta V_{bg} = V_{bg} - V_{\mathrm{peak},bg}$ [see Fig. 7(c)] [142]. The estimated effective electron temperature, T_e = 2.1 K, is close to the base temperature (of 2.0 K) of the cryostat, leading to the conclusion that the peak broadening is mainly limited by temperature rather than by the lifetime of the resonant state.

4.1.1 Transport gap in back gate

One way of quantifying the size of the transport gap in back gate voltage ΔV_{bg} is shown in Fig. 7(d) [and Fig. 7(e)]. Here, the conductance trace is smoothened over a back gate voltage range large enough to eliminate the (reproducible) resonances without affecting the general shape (compare gray and black trace). The regions of a linear increase of the conductance at both sides of the transport gap are selected, and a linear fit is performed (dashed bold lines). The gap size in back gate voltage ΔV_{bg} is then defined as the distance between the intersection points of the fitted traces with the $G = 0$ line (ΔV_{bg} = 3.4 V). This is a reasonable approach since the conductance values are much smaller than the minimal conductivity observed for extended graphene systems, which is of the order of $4e^2/h$ [see e.g., Fig. 2(a)]. Also, different approaches to define the gap have been applied, for example by defining a cutoff current. However, the over-

all results are the same, even if the details are changed slightly [124].

The corresponding energy scale ΔE_F related to ΔV_{bg} can be estimated from $\Delta E_F \approx \hbar v_F \sqrt{2\pi C_g \Delta V_{bg}/|e|}$, where C_g is the back gate capacitance per area [125]. For the measurements shown in Figs. 7(a) and (d), we find for example an energy gap $\Delta E_F \approx 110 - 340$ meV which is more than one order of magnitude larger than $E_g = 8$ meV [see above and Fig. 7(d)]. This discrepancy is attributed to different physical situations described by these two energy scales, which will be further discussed below (see Subsection 4.2).

4.1.2 Energy gap in bias direction

More insight into the energy gap in bias direction E_g [Fig. 7(e)] can be gained by focusing on a smaller back gate voltage range, as shown in Fig. 7(f), which are high-resolution differential conductance dI/dV_b close-ups of Fig. 7(e). At this scale, transport is dominated by well distinguishable (or intersecting) diamonds of suppressed conductance [see dashed lines in Fig. 7(f)] which indicate that transport is blocked by localized electronic states or quantum dots (see also Ref. [126]). The related charging energy E_c which is by itself related to the quantum dot size, depends on the Fermi energy in a small back gate voltage range [see e.g., different diamond sizes in Fig. 7(f)] but also on a large scale [see Fig. 7(e)]. It has been confirmed that the outline of Fig. 7(d) can indeed be obtained by plotting individually extracted charging energies as function of V_{bg} over a large back gate voltage range (see e.g. [125]).

In the following, the energy gap in bias direction E_g will be defined as the maximum charging energy $E_{c,max}$, which is directly related to the smallest charged island along the nanoribbon ever forming when the density is swept. More details will be given below.

4.1.3 Energy scales as function of geometry

In Fig. 8(a) we summarize the transport gaps in back gate voltage ΔV_{bg} [determined as shown in Fig. 7(d)] as function of w for different graphene samples consisting of different nanoribbons with width w and length l. The error bars in horizontal direction result from the resolution of the SFM scans, while the vertical error bars are determined by applying the procedures to different measurements of the same constriction, and using different ranges for smoothening and fitting. We see a decay of the gap size with increasing constriction width w, in good agreement with the observations by Han *et al.* [123] for the size of the transport gap in bias direction E_g. For the longer constrictions with $l = 200$ nm and especially $l = 500$ nm, ΔV_{bg} is larger than the value one would expect for a 100 nm long constriction of the same width w. This can be understood by the fact that increasing the width of the constriction or decreasing its length increases the probability of at least one percolating conductive path through the constriction, and therefore decreases the region in energy where transport is governed by localization [124]. Please note that for the constrictions with $w = 75$ nm and $l = 100$ nm, $w = 100$ nm and $l = 100$ nm, $w = 85$ nm and $l = 200$ nm, $\Delta V_{bg} < 0$. The value of ΔV_{bg} includes an offset which depends on the conductance value chosen to measure the distance between the fitted

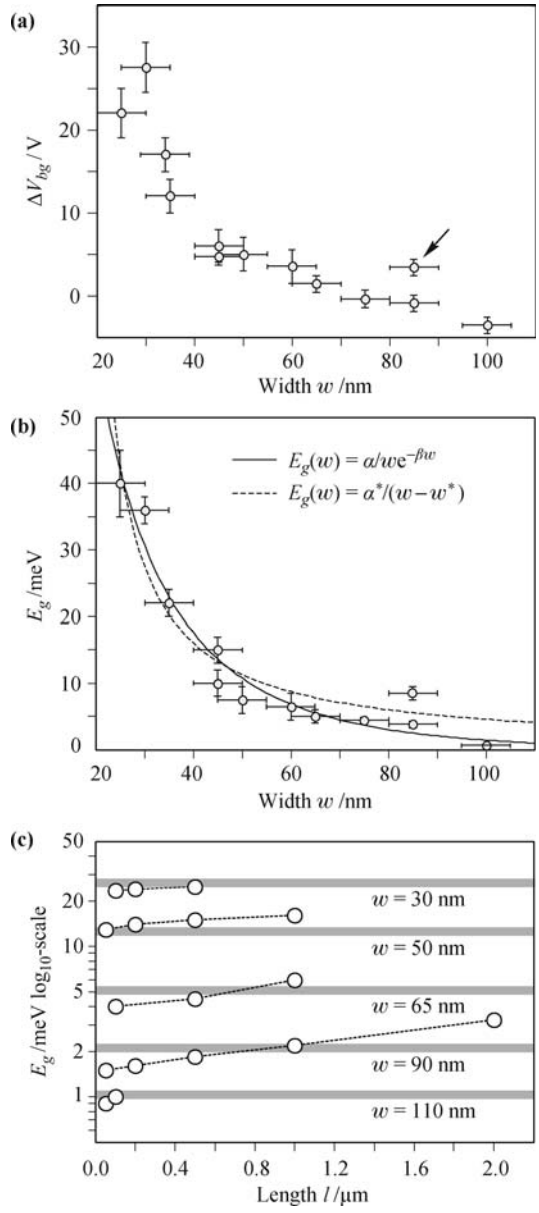

Fig. 8 **(a)** Transport gap in the back gate voltage ΔV_{bg} as function of (the minimum) width w for 12 different graphene nanoribbon and nanoribbon-like devices. **(b)** The corresponding energy gap E_g as a function of width. The experimental data can be well described by two-parameter models as shown by the solid and dashed lines. For more information please see text. **(c)** Energy gap E_g as a function of length l for a number of different graphene constrictions with different widths w (see labels and data points connected by dashed lines). The horizontal gray lines represent $E_g = \alpha/we^{-\beta w}$, where α=2 eV and β=0.026 nm^{-1}.

lines. With the choice of taking the intersection at $G = 0$, a negative value of ΔV_{bg} means that the intersection point of the two fitted lines lies at a positive conductance value. In these cases, even though the conductance is reduced due to localized states in the constriction, it is never completely suppressed [124].

In Fig. 8(b) we summarize the energy gaps measured in source drain bias direction E_g [estimated as shown, e.g., in Fig. 7(e)] as function of w for a number of different samples with different geometries, and different minimum width w, and length l. The error bars in horizontal direction again result from the SFM scans, while the vertical error bars are determined from the scatter of the charging energies extracted from Coulomb blockade diamond measurements as shown above. We observe a decreasing energy gap E_g with increasing constriction width w, in good agreement with the observations by Han *et al.* [123]. Indeed, despite the different fabrication process (Han and colleagues use hydrogen silsesquioxane (HSQ) as the resist, and do not remove it prior to the measurements), good agreement also on a quantitative level has been found. For example, we can fit our data in Fig. 8(b) by $E_g(w) = \alpha^*/(w - w^*)$, where $\alpha^* = 0.38$ eV·nm, and $w^* = 16$ nm accounts for inactive edges [123]. These values are in good agreement with those reported by Han *et al.* [123] and moreover, we also observe the systematic overestimation of E_g for wider ($w > 60$ nm) graphene nanoribbons. Following Sols *et al.* [140] the energy gap may be interpreted as the renormalized charging energy of strongly coupled quantum dots. In the frame of their model we can fit the energy gap by $E_g(w) = \alpha/w\mathrm{e}^{-\beta w}$, and find $\alpha = 2$ eV nm and $\beta = 0.026$ nm^{-1} [see solid line in Fig. 8(b)], again in good agreement with Ref. [140].

Figure 8(c) displays the extracted energy gaps E_g as a function of the length for five different widths. It can be seen that E_g-strongly depends on the width and we find good agreement with earlier experiments and theoretical models. In particular, we compare our results with the model from Ref. [140], where the energy gap is approximated by $E_g = \alpha/w\mathrm{e}^{-\beta w}$ [see gray bars in Fig. 8(c)]. Most importantly is the weak E_g-length dependence in this systems, which is in agreement with a rather simple picture described in the next subsection.

4.2 Coulomb blockade in nanoconstrictions

The experimental data shown above provide indications that the two experimentally observed energy scales E_g and ΔE_{F} are related to charged islands or quantum dots forming spontaneously along the nanoribbon. Similar observations were reported in Refs. [126, 127]. This is supported by the observation i) of Coulomb diamonds, which vary in size as function of the Fermi energy [Fig. 7(f)], ii) of a variation of the relative lever arms of individual resonances [125] and iii) of local islands charging inside the nanoribbon [124–126]. Quantum dots along the nanoribbon can arise in the presence of a quantum confinement energy gap (ΔE_{con}) combined with a strong bulk and/or edge-induced disorder potential Δ_{dis}, as illustrated in Fig. 9. The confinement energy can be estimated by $\Delta E_{\mathrm{con}}(w) = \gamma\pi a_{\mathrm{C-C}}/w$, where $\gamma \approx 2.8$ eV and $a_{\mathrm{C-C}} = 0.142$ nm [119]. This leads to $\Delta E_{\mathrm{con}} = 26$ meV for $w = 45$ nm, which by itself can neither explain the observed energy scale ΔE_{F}, nor the formation of quantum dots in the nanoribbon.

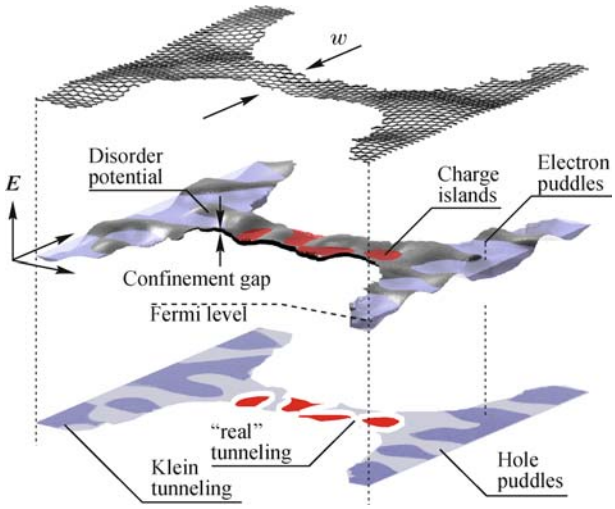

Fig. 9 Schematic illustration summarizing the mechanism behind the formation of charged islands and quantum dots in graphene nanoribbons. Graphene nanoribbon etched out of a two-dimensional graphene flake (as illustrated on the very top). A disorder potential (arising from both intrinsic and extrinsic effects) leads to the formation of electron and hole puddles in the near vicinity of the charge neutrality point (thus, at low-carrier densities). Since graphene has no band gap and carriers mimic relativistic particles Klein tunnelling and related phenomena make the boundary between electron and hole puddles reasonably transparent. The finite width w introduces a confinement gap (see the black line in the central panel), which isolates individual charge islands or quantum dots. Due to the confinement gap Klein tunnelling gets substituted by real tunneling as highlighted by the lower panel. Reproduced from Ref. [128], Copyright © 2010 Institute of Physics.

However, by superimposing a disorder potential giving rise to electron–hole puddles near the charge neutrality point [143], the confinement gap ensures that Klein tunneling (from electron puddle to hole puddle or vice versa) gets substituted by real tunneling. Within this model, ΔE_{F} depends on both the confinement energy gap and the disorder potential. An upper bound for the magnitude of the disorder potential can be estimated from ΔE_{F} extracted from the data presented above. Comparing to Ref. [143] where a bulk carrier density fluctuation of the order of $\Delta n \approx \pm 2 \times 10^{11}$ cm^{-2} was reported, we find reasonable agreement as the corresponding variation of the local potential is $\Delta E_{\mathrm{F}} \approx 126$ meV. We can estimate the fraction of overlapping diamonds by summing over all charging energies E_c extracted from measurements as e.g. shown in Fig. 7(f). It is expected that this

value depends strongly on the length of the nanoribbon in agreement with findings in Ref. [124]. The energy gap E_g in bias direction does not tell much about the magnitude of the disorder potential, but it is rather related to the sizes of the charged islands. In particular, the minimum island size is related to the maximum charging energy $E_{c,max}$. By using a simple capacitor disc model, we can estimate the effective charge island diameter by $d = e^2/(4\epsilon\epsilon_r E_c) \approx 100$ nm [where $\epsilon_r = (1+4)/2$], which exceeds the nanoribbon width w. Thus, in nanoribbons of different width the charging energy will scale with w giving the experimentally observed $1/w$ dependence of the energy gap in bias direction, as shown in Fig. 8(b) and Refs. [123, 124].

5 Graphene quantum dots

Quantum dots [144, 145] are small man-made structures in a solid, typically with sizes ranging from nanometers to a few microns, consisting of 10^3–10^9 atoms where the number of free electrons can be tuned over a wide range. The (quasi-0-D) confinement of the electrons in all three spatial directions results in a quantized energy spectrum [see also Fig. 1(f)] and quantum dots are therefore regarded as artificial atoms [146]. Quantum dots are not only interesting from a fundamental point of view but are also promising hosts for spin qubits [147], which have been recognized as potential building blocks for future quantum information technology. In semiconductor material systems (e.g., GaAs), in which quantum dot-based solid-state spin qubits are most advanced today [38, 148, 149], spin–orbit and hyperfine interactions have been identified as the main processes limiting spin decoherence times. Therefore, alternative materials for quantum dots (such as, e.g., silicon [150, 151], semiconducting carbon nanotubes [152, 153], or nanowires [154, 155]) attract interest as hosts for potential spin-qubits. Graphene and carbon materials in general are believed to have exceptionally long spin coherence times due to weak spin–orbit interactions (light weight of carbon) [35, 36] and the low nuclear spin concentration, arising from the $\approx 1\%$ natural abundance of ^{13}C suppresses hyperfine coupling [37]. In addition, graphene quantum dots allow elucidating the quantum-to-classical crossover in both regular and chaotic-confined billiard systems with massless particles [108, 156, 157]. However, confining electrons in graphene is challenging, mainly due to the gapless electronic structure [4] and phenomena related to Klein tunneling [22, 23]. Therefore, split gate techniques (e.g., [164]) well-known for semiconducting materials, to fabricate quantum dots are hard to apply. Moreover, it has been found difficult to apply SFM-based local oxidation [165] to single-layer graphene for defining quantum dots. However, it has been shown recently that cutting out nanostructures from 2-D graphene allows to structurally confine electrons [94, 104, 105, 108, 109, 126]. Actually, the functionality of graphene nanodevices can be engineered by designing the structure of the graphene flake [see e.g. Fig. 10(a)]. This will be shown with four different examples, discussing (5.1) a graphene single-electron transistor based on a width-modulated graphene nanoribbon, (5.2) graphene single-electron transistor device with a nearby graphene nanoribbon acting as charge detector, (5.3) by discussing a graphene nanodevice small enough so that quantum confinement effects start to play an important role, and (5.4) by a graphene double quantum dot device.

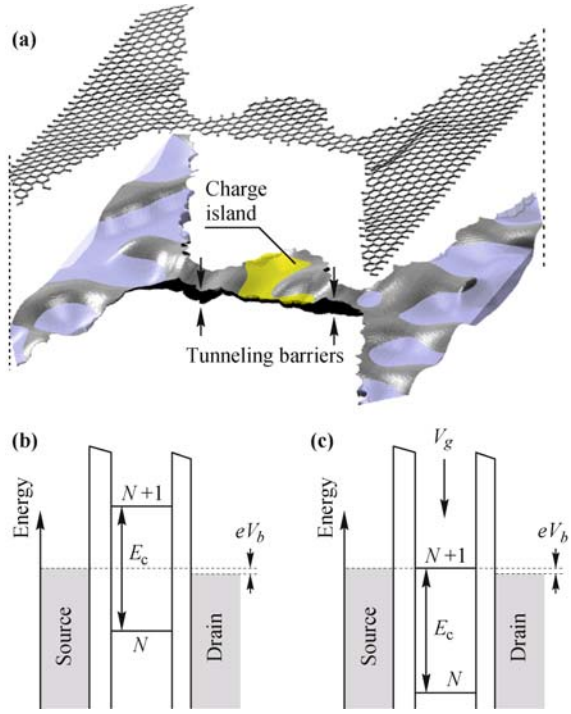

Fig. 10 **(a)** Schematic illustration of an etched graphene quantum dot, highlighting the formation of tunneling barriers and the charged island (similar to Fig. 9). **(b)** Illustration of energy levels in Coulomb blockade regime (off resonance). **(c)** By aligning an energy level of the island with the transport window the device is in resonance and transport becomes possible.

5.1 Graphene single electron transistor

Single electron transistors (SETs) [166], in general, consist of a conducting island connected by tunneling barriers to two conducting (source and drain) leads [see Fig. 10(a)] and (at least one) capacitively coupled gate to tune the potential on the island. Electronic transport through such devices (from source to drain) can be completely blocked by Coulomb interaction for temperatures and bias voltages lower than the characteristic energy required on adding an electron to the island [132, 166]. This is shown in Fig. 10(b). Since no energy level of the island lies inside the transport window (see dashed horizontal lines), the device is out of resonance and transport (i.e.,

current) is suppressed by the so-called Coulomb blockade. Here, temperature and bias (eV_b) are significantly smaller than the charging energy E_c. Additionally, it is assumed that the tunneling resistance of the two tunneling barriers is significantly larger than e^2/h, such that the island energy level broadening can be neglected [167]. By changing the gate potential, we can tune the single electron transistor into resonance, such that an island energy level is aligned within the transport window and carriers can resonantly hop from source to drain, as shown in Fig. 10(c).

The following discussion follows mainly the outline of Refs. [104, 105]. In Fig. 10(a), we show a schematic illustration of a tailored (i.e., etched) graphene flake providing the functionality of a graphene single electron transistor [94, 104–107]. The width modulated graphene nanostructure shown in Fig. 11(a) consists of a central island, two spatially separated constrictions, which act as effective tunnel barriers and three lateral graphene gates (the plunger gate PG and the barrier gates BG1 and BG2) are for full electrostatic tunability. It is crucial that narrow graphene constrictions (incl. nanoribbons) have been found to exhibit an effective transport gap [102, 122, 123, 140] enabling effective tunable tunneling barrier (see also Section 4). Although the transport gap is not a clean energy gap and is likely to be formed by a series of local quantum dots inside the nanoconstriction [124–127], the overall energy gap behavior can be modeled by the expression $E_g(w) = \alpha/we^{-\beta w}$ [140], as shown above. Thus, the exact shape of the effective energy gap, $E_g(x)$ (x is the transport direction) is given mainly by the lateral confinement, that is, by the variation of the width $w(x)$ along the device [see Fig. 10(a)]. By assuming that electron–hole symmetry holds in the confined geometry, we can extract the effective conduction band edge at $+E_g(x)/2$, and an effective valence band edge at $-E_g(x)/2$. Indeed, in this respect we can think of graphene band gap engineering by tailoring the graphene sheet width [123]. An alternative approach for realizing graphene single electron transistors is based on etched graphene nanoribbons and top gates for defining the actual charged islands, as shown and illustrated in Figs. 11(b) and (c).

In the following, we will discuss measurements recorded on width-modulated devices [e.g. Fig. 11(a)].

By adjusting the Fermi level [see lower panel in Fig. 10(a)] such that both effective band gaps are within the transport window, an electrically isolated island can be formed and transport can be tuned at the single-electron level. In Fig. 11(a), we show a (false color) SFM image of a fabricated graphene device consisting of a graphene flake tailored into a similar shape as shown in Fig. 10(a). The flake rests on approx. 300 nm SiO_2 and the highly doped Si substrate is used as a back gate to adjust the overall Fermi level. In Fig. 11(d) a low bias source-drain back gate characteristic of this device [Fig. 11(a)] is shown. The transport gap of strongly suppressed current (–25 V < V_{bg} < –12 V) separates the region of hole

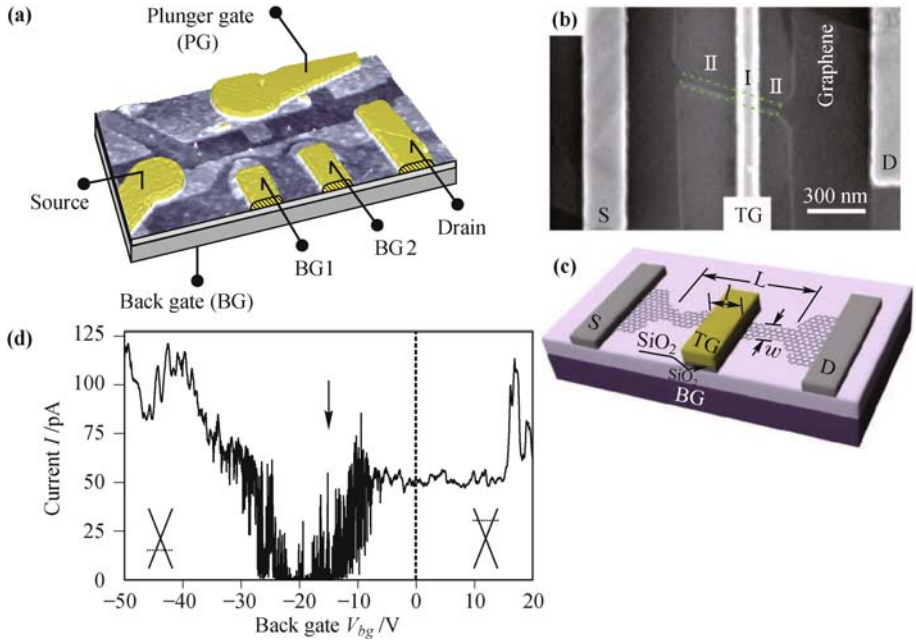

Fig. 11 **(a)** False color scanning force microscope image of an investigated graphene nanodevice. Bright areas mark the etched single layer graphene flake, whereas the elevated structures (in yellow) highlight the metal contacts. The minimum graphene feature size is approximately 50 nm. **(b)**, **(c)** Alternative graphene quantum dot design based on a top gated graphene nanoribbon, taken from Ref. [127]. The white scale bar in panel (b) corresponds to 300 nm. **(d)** Low bias source–drain back gate characteristic of the device shown in panel (a) at 1.7 K and V_b = 300 μV for $V_{b1} = V_{b2} = V_{PG} = 0$ V. The resolved transport gap separates between hole and electron transport as shown by the insets. Reproduced from Ref. [106], Copyright © 2009 World Scientific; Ref. [127], Copyright © 2009 American Physical Society.

(left side; see also inset) and electron (right side) transport. This transport characteristic is dominated by the two narrow constrictions, as also seen by direct comparison with Fig. 7(a). Fixing the back gate voltage (i.e., the Fermi level) to a value inside the transport gap, single electron transport phenomena can be investigated. Before focusing on the significantly smaller energy scale of the Coulomb blockade resonances, we discuss the full tunability on a larger energy scale. Figure 12(a) shows sourcedrain current measurements as function of applied barrier gate potentials (V_{b1} and V_{b2}) at fixed back gate [V_{bg} = –15 V; see arrow in Fig. 11(d)]. The bright areas represent regions of suppressed current, whereas in the corners (dark areas) we find either hole or electron-dominated transport. Vertical and horizontal stripes of suppressed current are observed, indicating that transport through each of the two constrictions is characterized by a transport gap, which can be individually tuned with the respective barrier gate. For example, keeping V_{b1} = –20 V constant and sweeping V_{b2} from –20 to +5 V keeps constriction 1 conducting whereas constriction 2 is tuned from large conductance to very low conductance (into the transport gap). The capacitive cross talk from barrier gate 1 (BG1) to constriction 2 and from barrier gate 2 (BG2) to constriction 1 has been found to be smaller than 2% [105].

Since the back gate voltage has been fixed [see arrow in Fig. 11(d)] such that the Fermi energy in the contacts of the structure lies within the conduction band, it can be indicated by horizontal dashed lines in the four drawings in Fig. 12(b). The four drawings represent energy diagrams corresponding to the four corners of Fig. 12(a), as indicated by the white numbers. For example, in corner 2 transport takes place in the conduction band throughout the whole structure. In corner 1 (4) transport occurs in the conduction band in the right (left) part of the structure. The left (right) constriction is traversed via states in the valence band. The situation is even more complex in corner 3, where the Fermi energy cuts both barrier regions in the valence band. Although these situations imply two or even four p–n-like transitions along the structure, no distinctive features are observed in these measurements. This may be a manifestation of the suppression of backscattering due to Klein tunneling [21]. These measurements [Fig. 12(a)] combined with the heuristic energy diagram model describing our sample [Fig. 12(b)] shows and explains the large tunability of the graphene nanodevice, where both tunneling barriers can be individually tuned over a large range including the crossover from hole to electron transport. In order to operate the device in the single electron transport configuration, we focus on a regime where both tunneling barriers are active (i.e., lie within the transport window). Thus, we focus, for example, on small barrier gate voltage regimes, as highlighted by the (labeled) dashed boxe in Fig. 12(a).

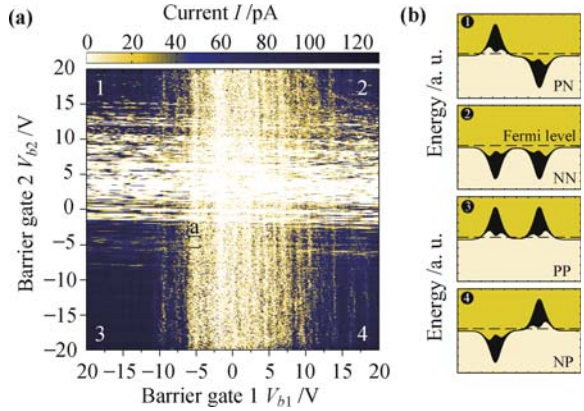

Fig. 12 Transport as function of the barrier gate potentials V_{b1}, V_{b2} and the back gate at small bias voltages. **(a)** Sourcedrain current plotted as function of V_{b1} and V_{b2} for constant back gate [V_{bg} = –15 V; see arrow in Fig. 11(d)]. Here, both individual gaps can clearly be seen. The white areas correspond to suppressed current. Please note also the gap homogeneity as a function of the back gate. **(b)** Schematic illustrations of the barrier configurations explaining the different transport regimes shown in panel (a). Reproduced from Ref. [105], Copyright © 2008 American Chemical Society.

In Fig. 13 we show such a close-up of transport characteristics in a regime. In general, we distinguish between the NN and the PP regimes, depending on either having the tunnel barriers (according to BG1 and BG2) shifted down (N) or up (P), as indicated in Fig. 12(b). We observe in all regimes sequences of horizontal and vertical stripes of suppressed current, and current resonances (for more details on different regimes see Refs. [105, 106]). Their direction in the V_{b1}–V_{b2} plane indicates that their physical origin has to be found within constriction 1 (vertical stripes) or constriction 2 (horizontal stripes). According to Section 3, some of these resonances can be understood as Coulomb blockade resonances of isolated charge islands inside the corresponding graphene constriction forming the effective tunneling barrier. A

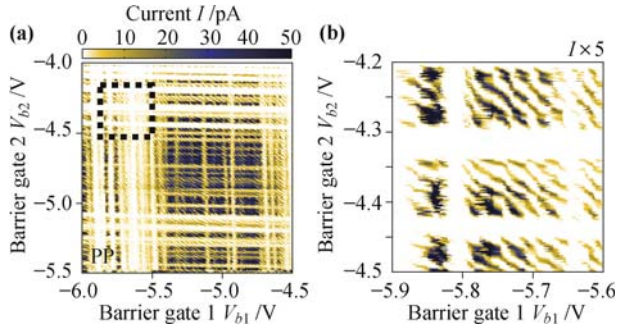

Fig. 13 Source–drain current through the graphene single-electron transistor as function of the barrier gates V_{b1} and V_{b2} for constant bias V_b = 300 μV and back gate V_{bg} = –15 V. **(a)** Close-up of Fig. 12(a) (as indicated therein by the labeled box), showing transport PP regimes. On top of the horizontal and vertical transmission modulations, we observe (diagonal) Coulomb blockade resonances. This is better seen in panel **(b)**, which is a close-up of panel (a). In panels (b) the current has been multiplied by factors of 5 to meet the color scale shown above panel (a). Reproduced from Ref. [105], Copyright © 2008 American Chemical Society.

blowup of a small region in Fig. 13(a) is shown in Fig. 13(b). The current exhibits even finer resonances which are almost equally well tuned by both constriction gates (see diagonal lines). These resonances are therefore attributed to states localized on the island between the barriers. It will be shown below that these resonances occur in the Coulomb blockade regime of the island. We attribute the deviations from perfectly straight diagonal lines to the presence of rough edges and inhomogeneities within the graphene island which has dimensions (slightly) larger than the elastic mean free path of the electrons [104]. This characteristic pattern [Fig. 13(b)] can be found within a large V_{b1}–V_{b2} parameter range within the regime where the two barrier gaps cross each other [i.e., the inner bright part of Fig. 12(a)].

So far we have mainly focused on the barriers. In the following, we concentrate on the charging of the island itself. We fix the barrier gate potentials (V_{b1} and V_{b2}) in the NP regime in order to study Coulomb blockade. Fig. 14(a) shows sharp conductance resonances with a characteristic period of about 20 mV (V_{b1} = 5.570 V and V_{b2} = –2.033 V are fixed). Their amplitude is modulated on a much larger voltage scale of about 200 mV by the transparency modulations of the constrictions (not shown). These resonances in the narrow graphene constrictions can significantly elevate the background of the Coulomb peaks. Figure 14(a), however, confirms that transport can also be completely pinched off between Coulomb blockade peaks. Corresponding Coulomb diamond measurements [166], that is, measurements of the differential conductance ($G_{\rm diff} = {\rm d}I/{\rm d}V_b$) as a function of bias voltage V_b and plunger gate voltage $V_{\rm PG}$ are shown in Fig. 14(b). Within the plunger gate voltage range shown, no charge rearrangements have been observed and the peak positions were stable over more than 10 consecutive plunger gate sweeps. It is found that the Coulomb peaks and the Coulomb diamonds are not very sensitive to the tunneling barrier regime, although in some cases p–n-like junctions are present, whereas in other cases a more uniform island might be expected.

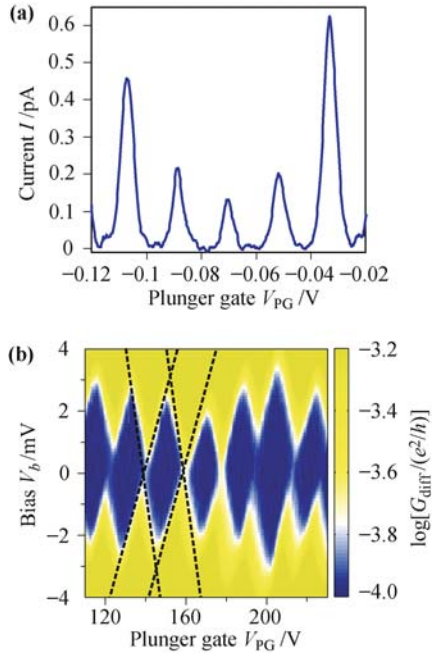

Fig. 14 **(a)** Coulomb peaks in current I as a function of plunger gate voltage $V_{\rm PG}$ (V_{bg} = –15 V, V_{b1} = 8.79 V, and V_{b2} = 8.85 V). **(b)** Coulomb diamonds in differential conductance $G_{\rm diff}$, represented in a logarithmic color scale plot (dark regions represent low conductance). A dc bias V_b with a small ac modulation (50 μV) is applied symmetrically across the dot and the current through the dot is measured. Coulomb diamonds have been measured in both the NP regime (panel a) and PP regime (panel b). Reproduced from Ref. [104], Copyright © 2008 American Institute of Physics; Ref. [105], Copyright © 2008 American Chemical Society.

5.2 Nanoribbon based charge detection on SETs

Next we discuss an integrated graphene device consisting of a graphene single electron transistor with a nearby graphene nanoribbon acting as a quantum point-contact-like charge detector. Charge detection techniques [172] have been shown to extend the experimental possibilities with single electron devices (incl. quantum dots) significantly. They are, powerful for detecting individual charging events and spin–qubit states [38, 148] and molecular states in coupled quantum dots [169]. Furthermore, charge detectors have been successfully used to investigate shot noise on the single electron level, and full counting statistics [170]. This makes charge detection also interesting for advanced investigation of graphene quantum dots and graphene nanodevices in general. Figure 15(a) shows a SFM image of an integrated graphene device consisting of a graphene single electron transistor with a graphene nanoribbon nearby. The single electron transistor device consists of two 25–30 nm wide and 75-nm long graphene constrictions separating source (S) and drain (D) contacts from the graphene quantum dot (QD). The diameter of the graphene island is approximately 100 nm. The constrictions and the island are electrostatically tuned independently again by two barrier gates (BG1 and BG2) and a central gate (CG), respectively. The highly doped silicon back gate (BG) allows again to adjust the overall Fermi level. In addition, we placed a 30 nm wide graphene nanoribbon approximately 35 nm next to the island, which acts as a charge detector, as shown below. The individual back gate characteristic of both devices is shown in Figs. 15(b) and (c). Here we show the source–drain current $I_{\rm sd}$ as a function of the back gate voltage (at a temperature of approximately 4 K) of both the single electron transistor (upper curve) and the charge detector (lower curve). In both cases we observe a transport gap above roughly 50 V. The large-scale current fluctuations are again attributed to resonances in the graphene constrictions. By focusing on a smaller back gate voltage

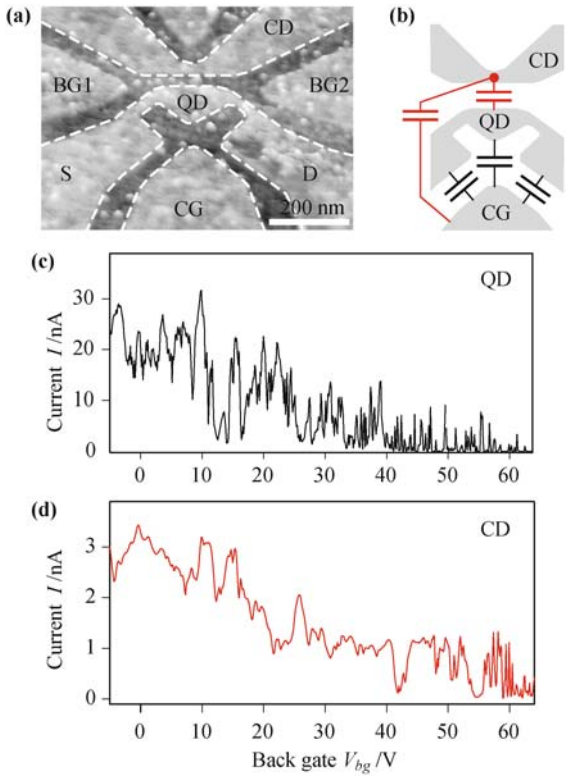

Fig. 15 **(a)** SFM image of the graphene quantum dot device with charge detector. The dashed lines highlight the contour of the graphene regions. The white scale bar corresponds to 200 nm. **(b)** Illustration of the main capacitive coupling involved in the measurements. **(c)** Back gate characteristics of the single electron transistor upper panel and the charge detector lower panel. The measurements were performed at a source–drain bias voltage of $V_{b,\mathrm{SET}} = 2$ mV and $V_{b,\mathrm{cd}} = 0.5$ mV at $T \approx 4$ K.

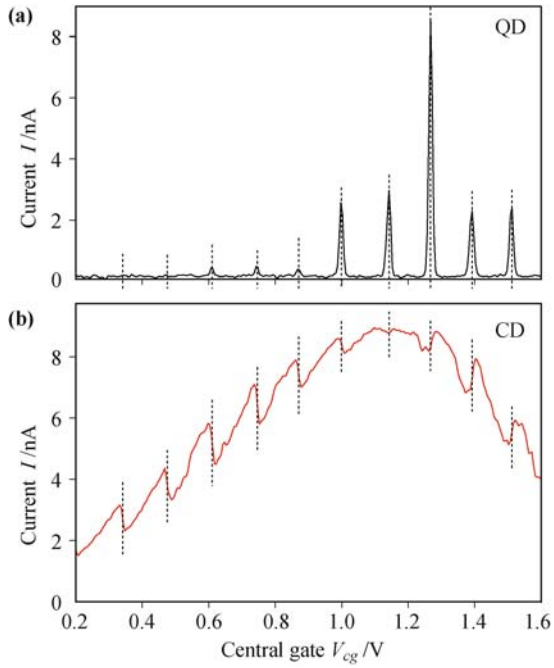

Fig. 16 Current through the **(a)** Single electron transistor (SET) I_{SET} and through the **(b)** charge detector I_{CD} as a function of central gate. The back gate is fixed at $V_{bg} = 60$ V at a temperature of $T \approx 1$ K. For each coulomb resonance peak in the dot signal there is a shift in the detector signal. These shifts even exist when the current through the dot is as low as the noise. The measurements are done with a dot bias $V_{b,\mathrm{SET}} = 500$ μV and a detector bias $V_{b,\mathrm{CD}} = 500$ μV.

range of 1 V (not shown). Coulomb blockade resonances of the single electron transistor (SET) and large-scale current fluctuations attributed to resonances in the tunnel barriers (TB) and charge detector (CD) are resolved. From this measurement the relative lever arms $\alpha_{\mathrm{CG,SET}}/\alpha_{\mathrm{BG,SET}} = 0.266$, $\alpha_{\mathrm{CG,TB}}/\alpha_{\mathrm{BG,TB}} = 0.197$ and $\alpha_{\mathrm{CG,CD}}/\alpha_{\mathrm{BG,CD}} = 0.030$ can be extracted. This is in agreement with the structure of the device since the barriers and the dot are closer to the central gate then the charge detector. After having demonstrated the functionality of both devices independently, their joint operation is shown in Figs. 16(a) and 17(b), where we demonstrate the functionality and sensitivity of the graphene charge detector. For these measurements the back gate voltage is set to $V_{bg} = 60$ V such that the Fermi level is close to the charge neutrality point as well as inside the transport gap of the charge detector.

Almost equidistantly spaced $\Delta V_{cg} = 129.5 \pm 7.3$ mV Coulomb blockade resonances are shown in Fig. 16(a) as a function of V_{cg} (at $V_{b,\mathrm{SET}} = 500$ μV). The strong modulation of the conductance peak amplitudes is due to superimposed resonances in the graphene constrictions defining the island. In Fig. 16(b) we plot the simultaneously measured conductance through the charge detector at a bias voltage of $V_{b,\mathrm{CD}} = 500$ μV for the same V_{cg} range. On top of the peak-shaped charge detector resonance we observe conductance steps that are well aligned (see vertical dotted lines) with single charging events on the island. Each conductance step is related to a shift in the charge detector resonance with respect to the central gate voltage. From an analysis of more than 30 charging events, an average shift in central gate voltage of $\Delta V_{cg,\mathrm{CD}} = 66.7 \pm 7.9$ mV is observed.

5.3 Electron–hole crossover in graphene quantum dots

By down-scaling the island of the single electron transistor device [see schematic in Fig. 10(a)] we step into a regime where quantum confinement effects dominate over classical Coulomb interaction effects [107]. Thus, for the detection of quantum confinement effects and the identification of individual orbital quantum states in graphene quantum dots, we move to smaller system sizes and lower temperatures. Here we discuss a graphene quantum dot device [see inset of Fig. 17(a)] consisting of a roughly 50-nm-wide and 80-nm-long quantum dot which is connected to source (S) and drain (D) via two 25 nm wide and 10-nm-long constrictions, acting as tunneling barriers. The dot and the leads can be tuned by an in-plane graphene plunger gate (PG) and the highly doped silicon substrate is used as a back gate (BG) to adjust the overall Fermi level. The following discussion follows

mainly the outline of Refs. [110, 111]. Again, the back gate voltage has been set close to the overall charge neutrality point of this graphene nanodevice. In Fig. 17(a) we show characteristic Coulomb blockade peaks (here as function of applied plunger gate voltage) measured inside the overall transport gap of this graphene quantum dot device. In contrast to Fig. 14(a), these resonances exhibit a much smaller linewidth (which is related to the significantly lower base temperature of approximately 90 mK) and a significantly larger peak spacing, which is due to the smaller size of the graphene island leading to both i) larger charging energy and ii) detectable quantum confinement (see below). The linewidth of these Coulomb blockade peaks has also been used to estimate an upper bound for the electronic temperature, which was found to be around 200 mK [110]. Characteristic Coulomb diamond measurements, i.e., differential conductance $G_{\rm QD} = {\rm d}I/{\rm d}V_b$, as a function of the quantum dot bias voltage V_b and plunger gate voltage $V_{\rm PG}$ are shown in Fig. 17(b). Within this plunger gate voltage range, no charge rearrangements were observed. Here, we extract a typical energy scale of the charging enregy on the order of 20 to 25 meV. This measurement has been recorded at a higher base temperature of $T \approx 370$ mK for providing a better visibility of the finestructure inside the diamond. The overall structure of the diamond is not changed significantly by increasing the temperature. The logarithmic plot of the Coulomb diamonds measured in the close vicinity of the charge neutrality point displays

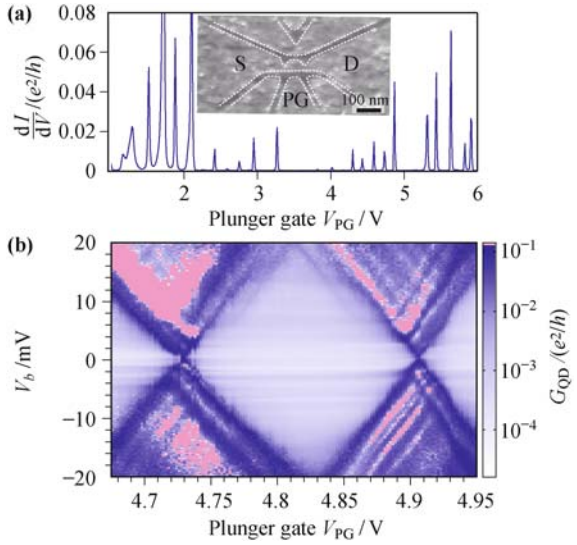

Fig. 17 **(a)** Coulomb blockade resonances of the graphene quantum as function of plunger gate voltage $V_{\rm PG}$ at $V_{bg} = -0.9\ V$. The conductance has been measured at constant bias of $V_b = 100\ \mu V$. The studied graphene quantum dot is shown in the inset. The scale bar corresponds to 100 nm. **(b)** Coulomb diamonds, i.e. finite-bias measurement of the QDs differential conductance $G_{\rm QD} = {\rm d}I/{\rm d}V_b$ as function of V_b and $V_{\rm PG}$ at $B = 0$. Note the rich excited state spectra and in particular the different vertical distances between the diamond edge and the diagonal structures inside the Coulomb-blockaded region for positive V_b. Reproduced from Ref. [111], Copyright © 2009 John Wiley & Sons, Inc.

a rich excited states spectrum. We observe lines of increased conductance outside the diamonds running parallel to the diamond edges, which are well aligned to inelastic cotunnelling onsets visible as faint horizontal (constant bias) structures inside the diamond-shaped regions. At the diamond boundary, the horizontal lines seamlessly join some of the most prominent diagonal lines in the non-blockaded region, allowing to extract characteristic excitation energies in the range of 2–5 meV. In addition, we observe for positive bias $V_b > 0$ V unconventional features inside the Coulomb-blockaded regions consisting of diagonal lines running parallel to the diamond edge. The fact that they have the same slope as the diamond edges suggests that they are connected to the alignment of an energy level with source (negative slope) or drain (positive slope). The vertical distance between the diagonal lines and the diamond edge is identical for lines with positive and negative slope. It has been shown by Schleser *et al.* [171] that these features are related to sequential tunnelling through the quantum dot, occurring after it has been excited by an inelastic cotunnelling process. In simple terms, these features can be attributed to a transport configuration where the tunnelling-out rate from the excited state is significantly larger than the relaxation rate to the ground state, which might be directly related to strongly nonlinear energy dependences of the tunnelling barriers.

In Fig. 18(a) we show about 50 Coulomb resonances as a function of a magnetic field B perpendicular to the sample plane. We tune from hole to electron transport since we cover the whole transport gap (not shown). The evolution of Coulomb resonances in the (perpendicular) magnetic field shows indications of the electron–hole crossover of the quantum dot states as we will explain below. There is a common trend of resonances at lower PG voltages (see e.g., the box at $V_{\rm PG} \approx 2.6$ V) to bend for increasing B-field towards higher energies (higher $V_{\rm PG}$). In contrast, we find for higher PG voltage regimes the opposite trend (see e.g., the box at $V_{\rm PG} \approx 6$ V), where resonances tend to shift to lower energies for increasing B-field. This overall pattern is disturbed by a number of additional features such as localized states, regions of multi-dot behavior and strong amplitude modulations probably due to constriction resonances. For example, we observe around $V_{\rm PG} = 3$ V a weakly coupled state crossing the resonances to the left at $B = 5$ and 9 T. At $B = 0$ T this state is not visible in transport but leads to a large diamond and an extended peak to peak spacing (not shown). We interpret the weak magnetic field dependence of this state and its low visibility in transport as a manifestation of a localized state possibly caused by disorder. Additionally, we observe several level crossings and splittings in the region of $V_{\rm PG}$ =5–6 V. This is consistent with the presence of additional resonances following a different PG/BG lever arm.

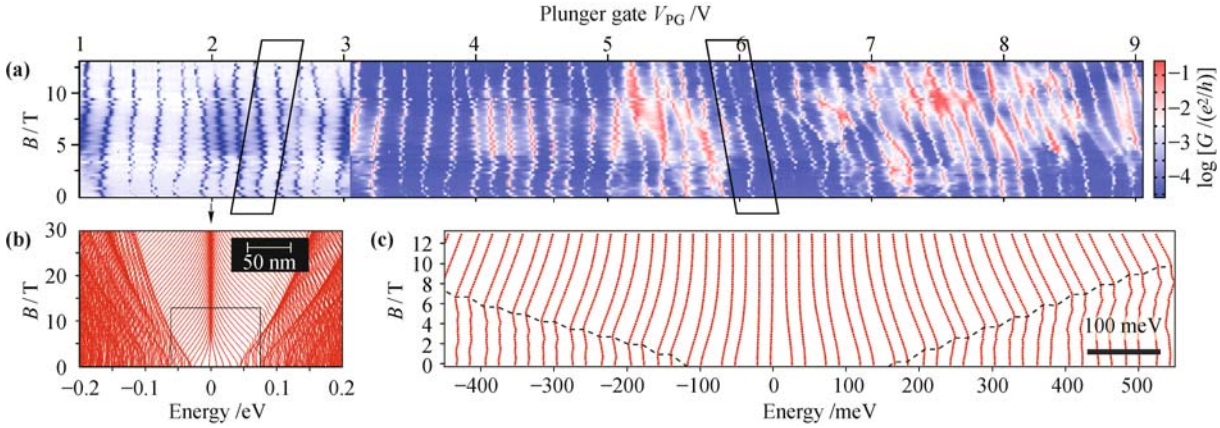

Fig. 18 **(a)** Evolution of Coulomb-blockade resonances in perpendicular magnetic field. The conductance is plotted as a function of plunger gate voltage $V_{\rm PG}$ and magnetic field B ($V_b = 100$ μV). **(b)** Calculated levels of a graphene quantum dot (see inset) as a function of magnetic field. Arrows mark the lowest Landau level (E_0), i.e., the electron–hole crossover at $n = 0$. **(c)** Close-up of dashed box in panel (b), where spin, Zeeman splitting and a constant charging energy of 18 meV are included. Reproduced from Ref. [110], Copyright © 2009 American Physical Society.

To further elucidate the evolution of the Coulomb resonances in the magnetic field, numerical calculations of the eigen energies of a graphene quantum dot in a perpendicular B-field have been performed. We use a third-nearest neighbor tight-binding approximation to simulate a 50×80 nm graphene quantum dot [see inset in Fig. 18(b)] containing ≈ 150 000 carbon atoms (for details on the numerical method see Refs. [157, 158]). The magnetic field is included by a Peierls phase factor [159]. To eliminate contributions from edge states localized at the zigzag-boundaries [160] we employ an alternating on-site potential of ±2 eV on all carbon atoms with dangling bonds.

Figure 18(b) shows that for zero magnetic field, the states lie sparsely around the Dirac point, and get more dense with increasing energy. As the magnetic field increases, the single-particle states converge asymptotically towards the two-dimensional Landau levels (LLs) at energies $E_n = \mathrm{sign}(n)\sqrt{2e\hbar v_{\rm F}^2|n|B}, \quad n \in \mathbb{Z}$. In particular, the LL at energy $E_0 = 0$ is formed [see arrow in Fig. 18(b)]. As a consequence, single-particle states around $E = 0$ evolve with magnetic field forming a simple pattern which is almost symmetric around $E = 0$. This is similar to the result of analytical calculations for a circular dot [161, 162]: for $|E| < E_1$ states slowly converge (for increasing B) towards E_0. This behavior is in contrast to energies $|E| > E_1$, which feature a complicated B-dependence as a result of many avoided level crossings. This effect is qualitatively robust against changes in the edge disorder and a moderate concentration of additional charged impurities. More details are presented in Ref. [158]. This behavior is a unique consequence of the linear 2-D-dispersion of graphene, and dissimilar to systems with parabolic dispersion.

In Fig. 18(c) we show a "close-up" of Fig. 18(b) (see dashed box therein), where additionally spin-degeneracy of each level and a constant charging energy $E_{\rm c}$ = 18 meV have been added to each single-particle level spacing. This value is estimated from corresponding Coulomb diamond measurements.

The mean single particle level spacing $\delta E \approx 4$ meV is significantly smaller than $E_{\rm c} \approx 18$ meV. Energy fluctuations (for increasing B) of the order of δE are therefore small on the energy scale shown in Fig. 18(a) and (c). At $E(B) = E_1$, however, states cross the first LL and start to converge towards E_0, resulting in kinks in the individual states [see dashed line in Fig. 18(c)].

The numerical data shows a qualitative correspondence to peak positions from the measurements in Fig. 18(a). Some kinks in the experimental data may be attributed to crossings with the first Landau level. Beyond the data presented here, these kinks in the magnetic field dependence of Coulomb resonances may be used in future experiments for identifying the few-electron regime in graphene. A similar method has been succesfully used in n-type GaAs lateral quantum dots [163].

5.4 Graphene double quantum dots

Beside of graphene single electron transistors and single quantum dot devices more recently also graphene double quantum dots [114–117] have been demonstrated succesfully. Such coupled double quantum dots have been proven to be particularly interesting candidates for the succesfull implementation of solid-state spin quibits [37]. In Fig. 19 we show two different realizations of a serial graphene double quantum dot [114, 116]. Figure 19(a) shows a SFM image of a device where the double quantum dot structure has been defined by the dry etching based "paper cutting" technique (described in Subsection 3.3). The left (L) and the right (R) quantum dot, both having a diameter of ≈ 90 nm, are connected by a 30 nm wide constriction and two additional 20 nm wide constrictions connect the two dots to the source (S) and

drain (D) lead. In total five lateral in-plane graphene gates and a global back gate can be used to tune the device. In Fig. 19(b) we show a different graphene double quantum dot device based on a single graphene nanoribbon (see dark dashed lines) and three top gates (G1, G2 and G3) for tuning the device into different transport regime [see also corresponding single quantum dot device in Figs. 11(b) and (c)]. In order to demonstrate the functionality of a graphene double quantum dot device we will show two charge stability diagram measurements recorded on the sample shown in Fig. 19(a).

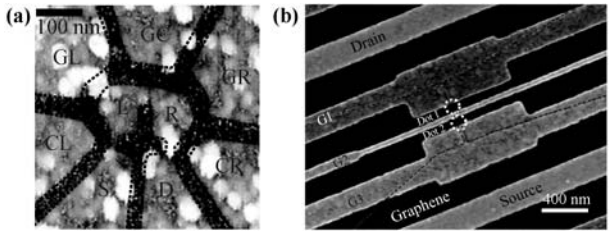

Fig. 19 **(a)** SFM scan of the graphene double dot sample presented in this chapter. The dashed lines highlight the contour of the graphene regions. **(b)** Scanning electron microscope image of a graphene nanoribbon based double quantum dot device. The dashed lines outline the graphene nanoribbon and the dotted lines indicate dot 1 and dot 2. Reproduced from Ref. [114], Copyright © 2009 American Institute of Physice; Ref. [116], Copyright © 2010 American Chemical Society.

In Fig. 20(a) we show a measurement of the current through the double quantum dot as a function of the voltages applied to the left and right gates (GL and GR) recorded at 1.4 K. The characteristic hexagonal charge stability diagram pattern typical for a double quantum dot [172] can be well observed. Current due to sequential tunneling through the two coupled dots is only possible at the so-called triple points, where the energy levels in both dots are aligned mutually and with the Fermi energy in the leads. In this logarithmic representation, a small current becomes also visible along the connecting lines between the triple points, which is due to cotunneling processes. Whenever a vertical line is passed, one electron enters or leaves the right dot, and crossing a horizontal cotunneling line removes or adds one electron to the left dot. The absolute carrier number in both dots is however not known. By applying a higher bias voltage over the double dot device, a finite window is allowed for the current flow, and the triple points develop into triangle-shaped regions. This can be even better seen by decreasing the electron temperature, such that the energy resolution increases as shown by the measurement presented in Fig. 20(b), which has been recorded at 120 mK. This measurement makes it possible to determine the lever arms and the energy scales characterising the system. We use the model of capacitively coupled dots to estimate the energy scales of the system, assuming that the applied source-drain voltage drops entirely over the double dot system. The extent of the triangular-shaped regions allow the determination of the conversion factors between gate voltage and energy. The lever arm between the left gate GL and the left dot is $\alpha_{\mathrm{GL,L}} = 0.17$ and between the right gate GR and the right dot $\alpha_{\mathrm{GR,R}} = 0.18$. The lever arms between the left gate and the right dot and vice-versa are determined from the slope of the lines delimiting the hexagons: $\alpha_{\mathrm{GL,R}} = 0.05$ and $\alpha_{\mathrm{GR,L}} = 0.06$. The dimensions of the honeycomb cells ΔV_{GL} and ΔV_{GR} give the single-dot charging energies $E_{\mathrm{c}}^{\mathrm{L}} = \alpha_{\mathrm{GL,L}} \cdot \Delta V_{\mathrm{GL}} = 13.2$ meV and $E_{\mathrm{c}}^{\mathrm{R}} = \alpha_{\mathrm{GR,R}} \cdot \Delta V_{\mathrm{GR}} = 13.6$ meV, which is comparable to the values found for graphene single dots of similar size [109]. Additional we observe finestructures inside the triple points, which are first indications that excited states also contributing to transport through this graphene double quantum dot device.

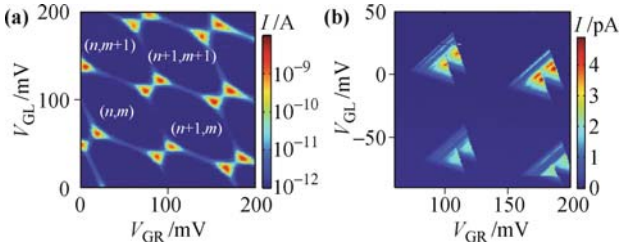

Fig. 20 **(a)** Color plot of the current through the double quantum dot shown in Fig. 19(a) as a function of the voltage applied to the in-plane gates V_{GR} and V_{GL}, displayed in logarithmic scale. The applied bias voltage is $V_b = 500$ μV. The electron occupation number in both dots are marked in white. **(b)** Current through the double quantum dot as a function of V_{GR} and V_{GL} measured at a higher bias voltage $V_b = 6$ mV and $T \approx 120$ mK. Reproduced from F. Molitor, PhD-Thesis, 2010.

6 Conclusions

In conclusion this review article shows the current status, the maturity and the versatility of quantum transport experiments on etched graphene nanostructured devices. Electronic properties and transport properties of bulk graphene have been revisited briefly and we have shown that by downscaling graphene devices their electronic properties get significantly altered. In contrast to bulk graphene, where pseudo-relativistic carriers and a semi-metallic band structure make it hard i) to confine carriers and ii) to fully pinched-off electron transport, nanostructured graphene enables strongly tunable electronic devices, such as tunneling barriers, single electron transistors, and quantum dots. The fabrication of etched graphene nanodevices has been described in detail and the preparation including etching techniques and the main characterization methods have been discussed, too. We have shown strong indications that in graphene nanodevices the formation of a disorder-induced energy gap replaces pseudo-relativistic “Klein” tunneling by “real” tunneling leading to the replacement of electron–hole puddles by fully isolated charged islands. These charged

islands or quantum dots are found to strongly dominate transport in etched graphene nanostructures. In particular, we discussed transport through graphene nanoribbons, single electron transistors, and quantum dots in detail. In all cases we explained the relevant energy scales related to the transport gaps, charging of the isolated islands, or quantum confinement effects.

These insights are important to understand transport in graphene nanostructures in general and may help in designing future graphene nanoelectronic devices with potential applications in the field of post-silicon nanoelectronics and quantum information technology. However, to compete with the sample quality of todays GaAs quantum dots and in particular with coupled quantum dots in this material graphene technology has to be improved significantly. For example, it is highly desirable to reduce the amount of disorder and the resulting parasitic localized states and edge states in graphene nanostructures. This currently highly active research area can be grouped in three directions: i) reduction of bulk disorder ii) reduction of edge disorder and iii) alternative ways to create a band gap or confine carriers in graphene:

(i) It has been shown, that a significant part of the bulk disorder results from the interaction of the graphene with the conventional SiO_2 substrate. Record carrier mobilities and the fractional quantum Hall effect could be observed by etching the oxide and suspending graphene [17, 19, 66, 67]. The suspension of graphene nanostructures allows to study the interplay of electrical with the unique mechanical properties of graphene. However, free standing structures are harder to gate and not only electrostatically but also mechanically delicate. An interesting alternative is the use of a different substrates such as hexagonal boron–nitride where the negative influence of the substrate is greatly reduced while containing the mechanical stability [16]. With both methods it remains important to limit the amount of contaminations and to use annealing procedures to remove as many residues as possible. The potential of clean devices is exemplary in carbon nanotubes, where a wealth of new phenomena could be observed in ultra-clean devices by growing the nanotubes as a last fabrication step [173, 174].

(ii) The reduction of bulk disorder alone might not be sufficient to significantly simplify the observations in graphene nanostructures. This is because all graphene nanostructures with sharp edges feature edge states around the charge neutrality point, except those with perfect armchair orientation. In order to construct atomically sharp edges bottom–up fabrication methods based on molecular precursors [175], unzipping of carbon nanotubes [176] or edge sensitive chemical cutting methods are proposed [177].

(iii) An other alternative is to find a different way to control charge carriers in graphene. It has been shown that a band gap can be opened in bilayer graphene due to breaking of the sublattice symmetry in an electric field [178, 179]. A remaining issue with this approach is the disorder which is comparable to the band gap and so far hinders complete electrical isolation. Chemical functionalization is an other promising route for the creation of a soft confinement [180, 181].

The big and still growing interdisciplinary community gives confidence that the current issues can be overcome and that measurements on devices of improved quality close to the state-of-the-art GaAs heterostructures allow to extract many more interesting details of confined quasi-particles in graphene quantum dots and allow to make use of the special physical properties in future graphene nanodevices.

Acknowledgements The authors wish to thank C. Barengo, P. Studerus (both ETH Zurich), M. Morgenstern, D. Grützmacher, P. Kordt, and J. Schirra for their support and help in setting up the new lab in Aachen. C. Stampfer acknowledges financial support by the JARA Seed Fund and the DFG (SPP-1459 and FOR-912).

References

1. R. Saito, G. Dresselhaus, and M. S. Dresselhaus, Physical Properties of Carbon Nanotubes, London: Imperial College Press, 2001
2. P. R. Wallace, Phys Rev., 1947, 71(9): 622
3. A. K. Geim and K. S. Novoselov, Nat. Mater., 2007, 6(3): 183
4. A. Castro-Neto, F. Guinea, N. M. Peres, K. S. Novoselov, and A. K. Geim, Rev. Mod. Phys., 2009, 81(1): 109
5. S. Reich, J. Maultzsch, C. Thomsen, and P. Ordejon, Phys. Rev. B, 2002, 66(3): 035412
6. J. W. McClure, Phys Rev., 1957, 108(3): 612
7. A. Castro-Neto, F. Guinea, and N. M. Peres, Phys. World, 2006, 19: 33
8. M. I. Katsnelson, Eur. J. Phys. B, 2006, 51(2): 157
9. M. I. Katsnelson and K. S. Novoselov, Solid State Commun., 2007, 143(1–2): 3
10. T. Ando, T. Nakanishia, and R. Saito, Microelectron. Eng., 1999, 47(1–4): 421
11. T. Ando and T. Nakanishi, J. Phys. Soc. Jpn., 1998, 67(5): 1704
12. K. S. Novoselov, A. K. Geim, S. V. Morozov, D. Jiang, M. I. Katsnelson, I. V. Grigorieva, S. V. Dubonos, and A. A. Firsov, Nature, 2005, 438(7065): 197
13. Y. Zhang, Y.-W. Tan, H. L. Stormer, and P. Kim, Nature, 2005, 438(7065): 201
14. S. Y. Zhou, G.-H. Gweon, J. Graf, A. V. Fedorov, C. D. Spataru, R. D. Diehl, Y. Kopelevich, D.-H. Lee, S. G. Louie, and A. Lanzara, Nat. Phys., 2006, 2(9): 595
15. A. Bostwick, T. Ohta, T. Seyller, H. K. Horn, and E. Rotenberg, Nat. Phys., 2007, 3(1): 36
16. C. R. Dean, A. F. Young, I. Meric, C. Lee, L. Wang, S. Sorgenfrei, K. Watanabe, T. Taniguchi, P. Kim, K. L. Shepard, and J. Hone, Nat. Nanotech., 2010, 5(10): 722
17. K. I. Bolotin, K. J. Sikes, J. Hone, H. L. Stormer, and P. Kim, Phys. Rev. Lett., 2008, 101(9): 096802

18. K. I. Bolotin, K. J. Sikes, Z. Jiang, G. Fundenberg, J. Hone, P. Kim, and H. L. Stormer, Solid State Commun., 2008, 146: 351
19. X. Du, I. Skachko, A. Barker, and E. Y. Andrei, Nat. Nanotech., 2008, 3: 491
20. E. V. Castro, H. Ochoa, M. I. Katsnelson, R. V. Gorbachev, D. C. Elias, K. S. Novoselov, A. K. Geim, and F. Guinea, Phys. Rev. Lett., 2010, 105(26): 266601
21. O. Klein, Z. Phys., 1929, 53(3–4): 157
22. N. Dombey and A. Calogeracos, Phys. Rep., 1999, 315(1–3): 41
23. M. I. Katsnelson, K. S. Novoselov, and A. K. Geim, Nat. Phys., 2006, 2(9): 620
24. A. Calogeracos and N. Dombey, Contemp. Phys., 1999, 40(5): 313
25. R. K. Su, G. C. Siu, and X. Chou, J. Phys. A, 1993, 26(4): 1001
26. V. G. Veselago, Sov. Phys. Usp., 1968, 10(4): 509
27. Y.-M. Lin, V. Perebeinos, Z. Chen, and P. Avouris, Phys. Rev. B, 2008, 78(16): 161409
28. K. S. Novoselov, Z. Jiang, Y. Zhang, S. V. Morozov, H. L. Stormer, U. Zeitler, J. C. Maan, G. S. Boebinger, P. Kim, and A. K. Geim, Science, 2007, 315(5817): 1379
29. T. Ando, T. Nakanishi, and R. Saito, J. Phys. Soc. Jpn., 1998, 67(8): 2857
30. M. V. Berry, Proc. R. Soc. Lond. A, 1984, 392(1802): 45
31. G. P. Mikitik and Y. V. Sharlai, Phys. Rev. Lett., 1999, 82(10): 2147
32. V. P. Gusynin, S. G. Sharapov, and J. P. Carbotte, Int. J. Mod. Phys. B, 2007, 21(27): 4611
33. A. K. Geim and P. Kim, Sci. Am., 2008, 298(4): 68
34. A. K. Geim, Science, 2009, 324(5934): 1530
35. D. Huertas-Hernando, F. Guinea, and A. Brataas, Phys. Rev. B, 2006, 74(15): 155426
36. H. Min, J. E. Hill, N. A. Sinitsyn, B. R. Sahu, L. Kleinman, and A. H. MacDonald, Phys. Rev. B, 2006, 74(16): 165310
37. B. Trauzettel, D. V. Bulaev, D. Loss, and G. Burkard, Nat. Phys., 2007, 3(3): 192
38. J. R. Petta, A. C. Johnson, J. M. Taylor, E. A. Laird, A. Yacoby, M. D. Lukin, C. M. Marcus, M. P. Hanson, and A. C. Gossard, Science, 2005, 309(5744): 2180
39. F. H. L. Koppens, C. Buizert, K. J. Tielrooij, I. T. Vink, K. C. Nowack, T. Meunier, L. P. Kouwenhoven, and L. M. K. Vandersypen, Nature, 2006, 442(7104): 766
40. C. Stampfer, J. Güttinger, F. Molitor, S. Schnez, E. Schurtenberger, A. Jacobsen, S. Hellmüller, T. Ihn, and K. Ensslin, book chapter in: Handbook of Nanophysics: Functional Nanomaterials, edited by K. D. Sattler, CRC Press, 2010
41. S. Datta, Electronic Transport in Mesoscopic Systems, Cambridge: Cambridge University Press, 1995
42. K. S. Novoselov, A. K. Geim, S. V. Morozov, D. Jiang, Y. Zhang, S. V. Dubonos, I. V. Grigorieva, and A. A. Firsov, Science, 2004, 306(5696): 666
43. C. Stampfer, F. Molitor, D. Graf, K. Ensslin, A. Jungen, C. Hierold, and L. Wirtz, Appl. Phys. Lett., 2007, 91(24): 241907
44. E. H. Hwang, S. Adam, and S. Das Sarma, Phys. Rev. Lett., 2007, 98(18): 186806
45. S. Ryu, L. Liu, S. Berciaud, Y. J. Yu, H. Liu, P. Kim, G. W. Flynn, and L. E. Brus, Nano Lett., 2010, 10(12): 4944
46. F. Molitor, J. Güttinger, C. Stampfer, D. Graf, T. Ihn, and K. Ensslin, Phys. Rev. B, 2007, 76(24): 245426
47. J. Meyer, A. K. Geim, M. I. Katsnelson, K. S. Novoselov, T. J. Booth, and S. Roth, Nature, 2007, 446(7131): 60
48. J. Moser, A. Barreiro, and A. Bachtold, Appl. Phys. Lett., 2007, 91(16): 163513
49. J. Martin, N. Akerman, G. Ulbricht, T. Lohmann, J. H. Smet, K. von Klitzing, and A. Yacoby, Nat. Phys., 2008, 4(2): 144
50. J. Tworzydlo, B. Trauzettel, M. Titov, A. Rycerz, and C. W. J. Beenakker, Phys. Rev. Lett., 2006, 96(24): 246802
51. Y.-W. Tan, Y. Zhang, K. Bolotin, Y. Zhao, S. Adam, E. H. Hwang, S. Das Sarma, H. L. Stormer, and P. Kim, Phys. Rev. Lett., 2007, 99(24): 246803
52. E. Fradkin, Phys. Rev. B, 1986, 33(5): 3263
53. A. W. W. Ludwig, M. P. A. Fisher, R. Shankar, and G. Grinstein, Phys. Rev. B, 1994, 50(11): 7526
54. N. M. R. Peres, F. Guinea, and A. H. Castro-Neto, Phys. Rev. B, 2006, 73(12): 125411
55. P. M. Ostrovsky, I. V. Gornyi, and A. D. Mirlin, Phys. Rev. B, 2006, 74(23): 235443
56. K. Ziegler, Phys. Rev. Lett., 1998, 80(14): 3113
57. F. Miao, S. Wijeratne, Y. Zhang, U. C. Coskun, W. Bao, and C. N. Lau, Science, 2007, 317(5844): 1530
58. R. Danneau, F. Wu, M. F. Craciun, S. Russo, M. Y. Tomi, J. Salmilehto, A. F. Morpurgo, and P. J. Hakonen, J. Low Temp. Phys., 2008, 153(5–6): 374
59. Z. Jiang, Y. Zhang, Y.-W. Tan, H. L. Stormer, and P. Kim, Solid State Commun., 2007, 143(1–2): 14
60. Z. Jiang, Y. Zhang, H. L. Stormer, and P. Kim, Phys. Rev. Lett., 2007, 99(10): 106802
61. V. K. Klitzing, G. Dorda, and M. Pepper, Phys. Rev. Lett., 1980, 45(6): 494
62. E. V. Gorbar, V. P. Gusynin, V. A. Miransky, and I. A. Shovkovy, Phys. Rev. B, 2002, 66(4): 045108
63. Y. Zheng and T. Ando, Phys. Rev. B, 2002, 65(24): 245420
64. V. P. Gusynin and S. G. Sharapov, Phys. Rev. Lett., 2005, 95(14): 146801
65. D. C. Tsui, H. L. Stormer, and A. C. Gossard, Phys. Rev. Lett., 1982, 48(22): 1559
66. X. Du, I. Skachko, F. Duerr, A. Luican, and E. Y. Andrei, Nature, 2009, 462(7270): 192
67. K. I. Bolotin, F. Ghahari, M. D. Shulman, H. L. Stormer, and P. Kim, Nature, 2009, 462(7270): 196
68. S. Franssila, Introduction to Micro Fabrication, Hoboken: John Wiley & Sons, 2004
69. T. Ohta, A. Bostwick, T. Seyller, K. Horn, and E. Rotenberg, Science, 2006, 313(5789): 951
70. C. Berger, Z. Song, X. Li, X. Wu, N. Brown, C. Naud, D. Mayou, T. Li, J. Hass, A. N. Marchenkov, E. H. Conrad, P. N. First, and W. A. de Heer, Science, 2006, 312(5777): 1191
71. P. W. Sutter, J.-I. Flege, and E. A. Sutter, Nat. Mater., 2008, 7(5): 406
72. K. S. Kim, Y. Zhao, H. Jang, S. Y. Lee, J. M. Kim, K. S. Kim, J. H. Ahn, P. Kim, J. Choi, and B. H. Hong, Nature, 2009, 457(7230): 706
73. X. Li, W. Cai, J. An, S. Kim, J. Nah, D. Yang, R. Piner, A. Velamakanni, I. Jung, E. Tutuc, S. K. Banerjee, L. Colombo, and R. S. Ruoff, Science, 2009, 324(5932): 1312
74. G. Eda, G. Fanchini, and M. Chhowalla, Nat. Nanotech., 2008, 3(5): 270
75. C. Stampfer, A. Bürli, A. Jungen, and C. Hierold, Physica Status Solidi B, 2007, 244(11): 4341

76. A. C. Ferrari, J. C. Meyer, V. Scardaci, C. Casiraghi, M. Lazzeri, F. Mauri, S. Piscanec, Da. Jiang, K. S. Novoselov, S. Roth, and A. K. Geim, Phys. Rev. Lett., 2006, 97: 187401
77. A. Gupta, G. Chen, P. Joshi, S. Tadigadapa, and P. C. Eklund, Nano Lett., 2006, 6(12): 2667
78. D. Graf, F. Molitor, K. Ensslin, C. Stampfer, A. Jungen, H. Hierold, and L. Wirtz, Nano Lett., 2007, 7(2): 238
79. D. S. L. Abergel, A. Russell, and V. Falko, Appl. Phys. Lett., 2007, 91(6): 063125
80. P. Blake, K. S. Novoselov, A. H. Castro Neto, D. Jiang, R. Yang, T. J. Booth, A. K. Geim, and E. W. Hill, Appl. Phys. Lett., 2007, 91(6): 063124
81. S. Roddaro, P. Pingue, V. Piazza, V. Pellegrini, and F. Beltram, Nano Lett., 2007, 7: 2707
82. C. Casiraghi, A. Hartschuh, A. E. Lidorikis, H. Qian, H. Harutyunyan, T. Gokus, K. S. Novoselov, and A. C. Ferrari, Nano Lett., 2007, 7: 2711
83. S. Pisana, M. Lazzeri, C. Casiraghi, K. S. Novoselov, A. K. Geim, A. C. Ferrari, and F. Mauri, Nat. Mater., 2007, 6(3): 198
84. S. Reich, C. Thomsen, and J. Maultzsch, Carbon Nanotubes: Basic Concepts and Physical Properties, Berlin: Wiley-VCH, 2004
85. M. S. Dresselhaus, G. Dresselhaus, A. Jorio, A. G., Souza, and R. Saito, Carbon, 2002, 40: 2043
86. A. C. Ferrari, Solid State Commun., 2007, 143(1–2): 47
87. C. Casiraghi, S. Pisana, K. S. Novoselov, A. K. Geim, and A. C. Ferrari, Appl. Phys. Lett., 2007, 91(23): 233108
88. J. Fernandez-Rossier, J. J. Palacios, and L. Brey, Phys. Rev. B, 2007, 75(20): 205441
89. A. Das, S. Pisana, B. Chakraborty, S. Piscanec, S. K. Saha, U. V. Waghmare, K. S. Novoselov, H. R. Krishnamurthy, A. K. Geim, A. K. Sood, and A. C. Ferrari, Nat. Nanotech., 2008, 3(4): 210
90. S. Berciaud, S. Ryu, L. E. Brus, and T. F. Heinz, Nano Lett., 2009, 9(1): 346
91. C. Thomsen and S. Reich, Phys. Rev. Lett., 2000, 85(24): 5214
92. J. Maultzsch, S. Reich, C. Thomsen, S. Webster, R. Czerw, D. L. Carroll, S. M. C. Vieira, P. R. Birkett, and C. A. Rego, Appl. Phys. Lett., 2002, 81(14): 2647
93. D. Bischoff, J. Güttinger, S. Dröscher, T. Ihn, K. Ensslin, and C. Stampfer, J. Appl. Phys., 2011, 109(7): 073710
94. J. Güttinger, C. Stampfer, S. Hellmüller, F. Molitor, T. Ihn, and K. Ensslin, Appl. Phys. Lett., 2008, 93(21): 212102
95. Y. Aharonov and D. Bohm, Phys. Rev., 1959, 115(3): 485
96. S. Russo, J. B. Oostinga, D. Wehenkel, H. B. Heersche, S. Shams Sobhani, L. M. K. Vandersypen, and A. F. Mopurgo, Phys. Rev. B, 2008, 77(8): 085413
97. M. Huefner, F. Molitor, A. Jacobsen, A. Pioda, C. Stampfer, K. Ensslin, and T. Ihn, Physica Status Solidi B, 2009, 246(11–12): 2756
98. M. Huefner, F. Molitor, A. Jacobsen, A. Pioda, C. Stampfer, K. Ensslin, and T. Ihn, New J. Phys., 2010, 12(4): 043054
99. Y. Wang, Y. Ouyang, X. Li, G. Wang, J. Guo, and H. Dai, Phys. Rev. Lett., 2008, 100(20): 206803
100. Q. Zhang, T. Fang, H. Xing, A. Seabaugh, and D. Jena, IEEE Electron Device Lett., 2008, 29(12): 1344
101. I. Meric, M. Y. Han, A. F. Young, B. Oezyilmaz, P. Kim, and K. Shepard, Nat. Nanotech., 2008, 3(11): 654
102. X. Li, X. Wang, L. Zhang, S. Lee, and H. Dai, Science, 2008, 319(5867): 1229
103. L. Liao, J. Bai, R. Cheng, Y.-C. Lin, S. Jiang, Y. Huang, and X. Duan, Nano Lett., 2010, 10(5): 1917
104. C. Stampfer, J. Güttinger, F. Molitor, D. Graf, T. Ihn, and K. Ensslin, Appl. Phys. Lett., 2008, 92(1): 012102
105. C. Stampfer, E. Schurtenberger, F. Molitor, J. Güttinger, T. Ihn, and K. Ensslin, Nano Lett., 2008, 8(8): 2378
106. C. Stampfer, E. Schurtenberger, F. Molitor, J. Güttinger, T. Ihn, and K. Ensslin, Int. J. Mod. Phys. B, 2009, 23(12–13): 2647
107. T. Ihn, J. Güttinger, F. Molitor, S. Schnez, E. Schurtenberger, A. Jacobsen, S. Hellmüller, T. Frey, S. Dröscher, C. Stampfer, and K. Ensslin, Materials Today, 2010, 13(3): 44
108. L. A. Ponomarenko, F. Schedin, M. I. Katsnelson, R. Yang, E. H. Hill, K. S. Novoselov, and A. K. Geim, Science, 2008, 320(5874): 356
109. S. Schnez, F. Molitor, C. Stampfer, J. Güttinger, I. Shorubalko, T. Ihn, and K. Ensslin, Appl. Phys. Lett., 2009, 94(1): 012107
110. J. Güttinger, C. Stampfer, F. Libisch, T. Frey, J. Burgdörfer, T. Ihn, and K. Ensslin, Phys. Rev. Lett., 2009, 103(4): 046810
111. J. Güttinger, C. Stampfer, T. Frey, T. Ihn, and K. Ensslin, Physica Status Solidi B, 2009, 246(11–12): 2553
112. J. Moser and A. Bachtold, Appl. Phys. Lett., 2010, 95(17): 173506
113. J. Güttinger, T. Frey, C. Stampfer, T. Ihn, and K. Ensslin, Phys. Rev. Lett., 2010, 105(11): 116801
114. F. Molitor, S. Dröscher, J. Güttinger, A. Jacobson, C. Stampfer, T. Ihn, and K. Ensslin, Appl. Phys. Lett., 2009, 94(22): 222107
115. F. Molitor, H. Knowles, S. Dröscher, U. Gasser, T. Choi, P. Roulleau, J. Güttinger, A. Jacobson, C. Stampfer, K. Ensslin, and T. Ihn, Europhys. Lett., 2010, 89(6): 67005
116. X. L. Liu, D. Hug, and L. Vandersypen, Nano Lett., 2010, 10(5): 1623
117. L.-J. Wang, H.-O. Li, Z. Su, T. Tu, G. Cao, C. Zhou, X.-J. Hao, G.-C. Guo, and G.-P. Guo, arXiv:1011.5347v1, 2010
118. L. Brey and H. A. Fertig, Phys. Rev. B, 2006, 73(23): 235411
119. C. T. White, J. Li, D. Gunlycke, and J. W. Mintmire, Nano Lett., 2007, 7(3): 825
120. K. Wakabayashi, Y. Takane, and M. Sigrist, Phys. Rev. Lett., 2007, 99(3): 036601
121. K. Wakabayashi, Y. Takane, M. Yamamoto, and M. Sigrist, Carbon, 2009, 47(1): 124
122. Z. Chen, Y.-M. Lin, M. Rooks, and P. Avouris, Physica E, 2007, 40(2): 228
123. M. Y. Han, B. Özyilmaz, Y. Zhang, and P. Kim, Phys. Rev. Lett., 2007, 98: 206805
124. F. Molitor, A. Jacobsen, C. Stampfer, J. Güttinger, T. Ihn, and K. Ensslin, Phys. Rev. B, 2009, 79(7): 075426
125. C. Stampfer, J. Güttinger, S. Hellmüller, F. Molitor, K. Ensslin, and T. Ihn, Phys. Rev. Lett., 2009, 102(5): 056403
126. K. Todd, H. T. Chou, S. Amasha, and D. Goldhaber-Gordon, Nano Lett., 2009, 9(1): 416
127. X. L. Liu, J. Oostinga, A. Morpurgo, and L. Vandersypen, Phys. Rev. B, 2009, 80(12): 121407
128. F. Molitor, C. Stampfer, J. Güttinger, A. Jacobsen, T. Ihn, and K. Ensslin, Semicond. Sci. Technol., 2010, 25(3): 034002
129. P. Gallagher, K. Todd, and D. Goldhaber-Gordon, Phys. Rev. B, 2010, 81(11): 115409
130. M. Y. Han, J. C. Brant, and P. Kim, Phys. Rev. Lett., 2010, 104(5): 056801

131. B. Terrés, J. Dauber, C. Volk, S. Trellenkamp, U. Wichmann, and C. Stampfer, Appl. Phys. Lett., 2011, 98(6): 032109
132. T. Heinzel, Mesoscopic Electronics in Solid State Nanostructures, Weinheim: Wiley-VCH, 2003
133. N. M. R. Peres, A. H. Casrtro-Neto, and F. Guinea, Phys. Rev. B, 2006, 73(19): 195411
134. D. Dunlycke, D. A. Areshkin, and C. T. White, Appl. Phys. Lett., 2007, 90: 142104
135. J. Fernandez-Rossier, J. J. Palacios, and L. Brey, Phys. Rev. B, 2007, 75(20): 205441
136. L. Yang, C.-H. Park, Y.-W. Son, M. L. Cohen, and S. G. Louie, Phys. Rev. Lett., 2007, 99(18): 186801
137. Y.-W. Son, M. L. Cohen, and S. G. Louie, Phys. Rev. Lett., 2007, 99: 186801
138. E. R. Mucciolo, A. H. Castro Neto, and C. H. Lewenkopf, arXiv:0806.3777v1, 2008
139. S. Adam, S. Cho, M. S. Fuhrer, and S. Das Sarma, Phys. Rev. Lett., 2008, 101(4): 046404
140. F. Sols, F. Guinea, and A. H. Castro Neto, Phys. Rev. Lett., 2007, 99(16): 166803
141. M. Evaldsson, I. V. Zozoulenko, H. Y. Xu, and T. Heinzel, Phys. Rev. B, 2008, 78: R161407
142. C. W. J. Beenakker, Phys. Rev. B, 1991, 44(4): 1646
143. J. Martin, N. Akerman, G. Ulbricht, T. Lohmann, J. H. Smet, K. von Klitzing, and A. Yacoby, Nat. Phys., 2008, 4(2): 144
144. L. P. Kouwenhoven and C. M. Marcus, Phys. World, 1998, 11: 35
145. L. P. Kouwenhoven, D. G. Austing, and S. Tarucha, Rep. Prog. Phys., 2001, 64(6): 701
146. M. A. Kastner, Phys. Today, 1993, 46(1): 24
147. D. Loss and D. P. DiVincenzo, Phys. Rev. A, 1998, 57(1): 120
148. J. M. Elzerman, R. Hanson, L. H. Willems van Beveren, B. Witkamp, L. M. K. Vandersypen, and L. P. Kouwenhoven, Nature, 2004, 430(6998): 431
149. F. H. L. Koppens, C. Buizert, K. J. Tielrooij, I. T. Vink, K. C. Nowack, T. Meunier, L. P. Kouwenhoven, and L. M. K. Vandersypen, Nature, 2006, 442(7104): 766
150. S. J. Angus, A. J. Ferguson, A. S. Dzurak, and R. G. Clark, Nano Lett., 2007, 7(7): 2051
151. N. Shaji, C. B. Simmons, M. Thalakulam, L. J. Klein, H. Qin, H. Luo, D. E. Savage, M. G. Lagally, A. J. Rimberg, R. Joynt, M. Friesen, R. H. Blick, S. N. Coppersmith, and M. A. Eriksson, Nat. Phys., 2008, 4: 540
152. M. J. Biercuk, N. Mason, and C. M. Marcus, Nano Lett., 2004, 4(1): 1
153. S. Sapmaz, C. Meyer, P. Beliczynski, P. Jarillo-Herrero, and L. P. Kouwenhoven, Nano Lett., 2006, 6(7): 1350
154. C. Fasth, A. Fuhrer, M. T. Bjork, and L. Samuelson, Nano Lett., 2005, 5(7): 1487
155. I. Shorubalko, A. Pfund, R. Leturcq, M. T. Borgström, F. Gramm, E. Müller, E. Gini, and K. Ensslin, Nanotechnology, 2006, 18(4): 044014
156. M. V. Berry and R. J. Mondragon, Proc. R. Soc. Lond. A, 1987, 412: 53
157. F. Libisch, C. Stampfer, and J. Burgdörfer, Phys. Rev. B, 2009, 79(11): 115423
158. F. Libisch, S. Rotter, J. Gttinger, C. Stampfer, and J. Burgdrfer, Phys. Rev. B, 2010, 81(24): 245411
159. Y. H. Chiu, Y. H. Lai, J. H. Ho, D. S. Chuu, and M. F. Lin, Phys. Rev. B, 2008, 77(4): 045407
160. M. Fujita, K. Wakabayashi, K. Nakada, and K. Kusakabe, J. Phys. Soc. Jpn., 1996, 65(7): 1920
161. S. Schnez, K. Ensslin, M. Sigrist, and T. Ihn, Phys. Rev. B, 2008, 78(19): 195427
162. P. Recher, J. Nilsson, G. Burkard, and B. Trauzettel, Phys. Rev. B, 2009, 79(8): 085407
163. M. Ciorga, A. S. Sachrajda, P. Hawrylak, C. Gould, P. Zawadzki, S. Jullian, Y. Feng, and Z. Wasilewski, Phys. Rev. B, 2000, 61(24): R16315
164. M. A. Reed, J. N. Randall, R. J. Aggarwal, R. J. Matyi, T. M. Moore, and A. E. Wetsel, Phys. Rev. Lett., 1988, 60(6): 535
165. S. Lüscher, A. Fuhrer, R. Held, T. Heinzel, K. Ensslin, and W. Wegscheider, Appl. Phys. Lett., 1999, 75(16): 2452
166. L. P. Kouwenhoven, C. M. Markus, P. L. McEuen, S. Tarucha, R. M. Westervelt, and N. S. Wingreen, Electron Transport in Quantum Dots, NATO ASI Conference Proceedings, edited by L. L. Sohn, L. P. Kouwenhoven, and G. Schön, 1997
167. T. Ihn, Springer Tracts in Modern Physics, 2004, 192: 102
168. M. Field, C. G. Smith, M. Pepper, D. A. Ritchie, J. E. F. Frost, G. A. C. Jones, and D. G. Hasko, Phys. Rev. Lett., 1993, 70(9): 1311
169. L. DiCarlo, H. Lynch, A. Johnson, L. Childress, K. Crockett, C. Marcus, M. Hanson, and A. C. Gossard, Phys. Rev. Lett., 2004, 92(22): 226801
170. S. Gustavsson, R. Leturcq, B. Simovic, R. Schleser, T. Ihn, P. Studerus, K. Ensslin, D. C. Driscoll, and A. C. Gossard, Phys. Rev. Lett., 2006, 96(7): 076605
171. R. Schleser, T. Ihn, E. Ruh, K. Ensslin, M. Tews, D. Pfannkuche, D. C. Driscoll, and A. C. Gossard, Phys. Rev. Lett., 2005, 94(20): 206805
172. W. G. van der Wiel, S. De Franceschi, J. Elzerman, T. Fujisawa, S. Tarucha, Rev. Mod. Phys., 2002, 75(1): 1
173. J. Cao, Q. Wang, and H. Dai, Nat. Mater., 2005, 4(10): 745
174. F. Kuemmeth, S. Ilani, D. Ralph, and P. McEuen, Nature, 2008, 452(7186): 448
175. J. Cai, P. Rueux, R. Jaafar, M. Bieri, T. Braun, S. Blankenburg, M. Muoth, A. Seitsonen, M. Saleh, X. Feng, K. Müllen, and R. Fasel, Nature, 2010, 466(7305): 470
176. L. Jiao, X. Wang, G. Diankov, H. Wang, and H. Dai, Nat. Nanotech., 2010, 5(5): 321
177. L. C. Campos, V. R. Manfrinato, J. D. Sanchez-Yamagishi, J. Kong, and P. Jarillo-Herrero, Nano Lett., 2009, 9(7): 2600
178. J. Oostinga, H. Heersche, X. Liu, A. Morpurgo, and L. Vandersypen, Nat. Mater., 2007, 7(2): 151
179. Y. Zhang, T. Tang, C. Girit, Z. Hao, M. Martin, A. Zettl, M. Crommie, Y. Shen, and F. Wang, Nature, 2009, 459(7248): 820
180. T. Echtermeyer, M. Lemme, M. Baus, B. Szafranek, A. Geim, and H. Kurz, Electron Device Letters IEEE, 2008, 29(8): 952
181. R. Nair, W. Ren, R. Jalil, I. Riaz, V. Kravets, L. Britnell, P. Blake, F. Schedin, A. Mayorov, S. Yuan, M. I. Katsnelson, H. M. Cheng, W. Strupinski, L. G. Bulusheva, A. V. Okotrub, I. V. Grigorieva, A. N. Grigorenko, K. S. Novoselov, and A. K. Geim, Small, 2010, 6(24): 2773